

PHYSICS

Distinguishability and “which pathway” information in multidimensional interferometric spectroscopy with a single entangled photon-pair

Shahaf Asban* and Shaul Mukamel*

Correlated photons inspire abundance of metrology-related platforms, which benefit from quantum (anti-) correlations and outperform their classical counterparts. While these mainly focus on entanglement, the role of photon exchange phase and degree of distinguishability has not been widely used in quantum applications. Using an interferometric setup, we theoretically show that, when a two-photon wave function is coupled to matter, it is encoded with “which pathway?” information even at low-degree of entanglement. An interferometric protocol, which enables phase-sensitive discrimination between microscopic interaction histories (pathways), is developed. We find that quantum light interferometry facilitates utterly different set of time delay variables, which are unbound by uncertainty to the inverse bandwidth of the wave packet. We illustrate our findings on an exciton model system and demonstrate how to probe intraband dephasing in the time domain without temporally resolved detection. The unusual scaling of multiphoton coincidence signals with the applied pump intensity is discussed.

INTRODUCTION

Interferometry introduces myriad of novel platforms to spectroscopy, aiming at revealing quantum information encoded in the wave function of multiple photons (1–6). One intriguing aspect of many-body quantum dynamics is the exchange statistics of indistinguishable particles, whereby the wave function acquires a phase upon the exchange of two particles. This affects their dynamics and is detectable via unique interference patterns in the correlations of two (or more) particles. Coincidence counting of photons (7), current correlations of electrons (8), and fractional charges (quantum Hall quasi-particles) (9, 10) are notable examples. In quantum electrodynamics, light-matter coupling can be represented as the sum of all possible interaction histories (pathways). These pathways differ by the temporal order of events; thus, multiphoton nonlinear processes are potentially imprinted with their relative phases. Although the exchange phase of photons is fixed and solely determined by their bosonic nature, it can be effectively manipulated using a well-established interferometric setup for a pair of entangled photons (11).

Here, we develop an exchange phase cycling scheme that scans through different values of such a phase. We then demonstrate the capacity of the multiphoton wave function to encode and decipher matter information inaccessible otherwise. Matter information gain is physically manifested in a reduced number of light-matter configurations, the ability to switch between them, and a new set of time delay variables with unique characteristics. We study the multidimensional spectral information generated by coupling an entangled photon pair to matter, via combination of interferometers, as depicted in Fig. 1. Our scheme includes two interferometric stages: state preparation interferometer, followed by a “reading” setup for the quantum state encoded by light-matter information exchange. This results in several notable differences in comparison to the familiar semiclassical

nonlinear optics. (i) While semiclassical techniques scan time delays between pulses, quantum interferometric setups introduce new type of time delay variables that are not conjugate to the wave packet bandwidth. (ii) Interferometric wave mixing (WM) of quantum light generates matter pathways unavailable classically due to the simultaneous detection of multiple photon propagation paths generated at different times (3). (iii) It allows the separation of pathways into groups while delivering phase-sensitive read of each process, unmatched by classical light. (iv) Coincidence detection obeys unique scaling relations between the applied intensity I_p , the light-sample coupling, and the detected signal. This allows to avoid damaging disturbance to the sample and eliminates unwanted signal contributions (background). (v) Coincidence counting singles out the two-photon subspace from the total signal, therefore, restricting the number of possible microscopic pathways. Consequently, two-photon signals are sensitive to collective excitations (harmonic and anharmonic), in contrast to single-photon counting that are generated by matter anharmonicities (12–14).

We propose an exchange phase cycling protocol that projects the information encoded in the multidimensional signals onto lower-dimension data, thereby revealing phase-dependent matter correlation functions. The interferometric time delays can probe the dephasing dynamics of the sample, without resorting to time-resolved detection. The latter is determined by the interferometer optical path difference and is not conjugate to the frequency measurement, paving the way to a high joint time-frequency resolution, beyond the Fourier limitation.

RESULTS

The setup

The interferometric spectroscopy setup depicted in Fig. 1 includes preparation and detection stages. Both play an essential role in acquisition of the nonlinear signal generated by the sample, through their control parameters. In the preparation process, a modified Michelson interferometer creates a photon pair with tunable degree

Copyright © 2021
The Authors, some
rights reserved;
exclusive licensee
American Association
for the Advancement
of Science. No claim to
original U.S. Government
Works. Distributed
under a Creative
Commons Attribution
NonCommercial
License 4.0 (CC BY-NC).

Downloaded from <https://www.science.org> at University of California Irvine on September 23, 2021

Department of Chemistry and Physics and Astronomy, University of California, Irvine, CA 92697-2025, USA.

*Corresponding author. Email: sasban@uci.edu (S.A.); smukamel@uci.edu (S.M.)

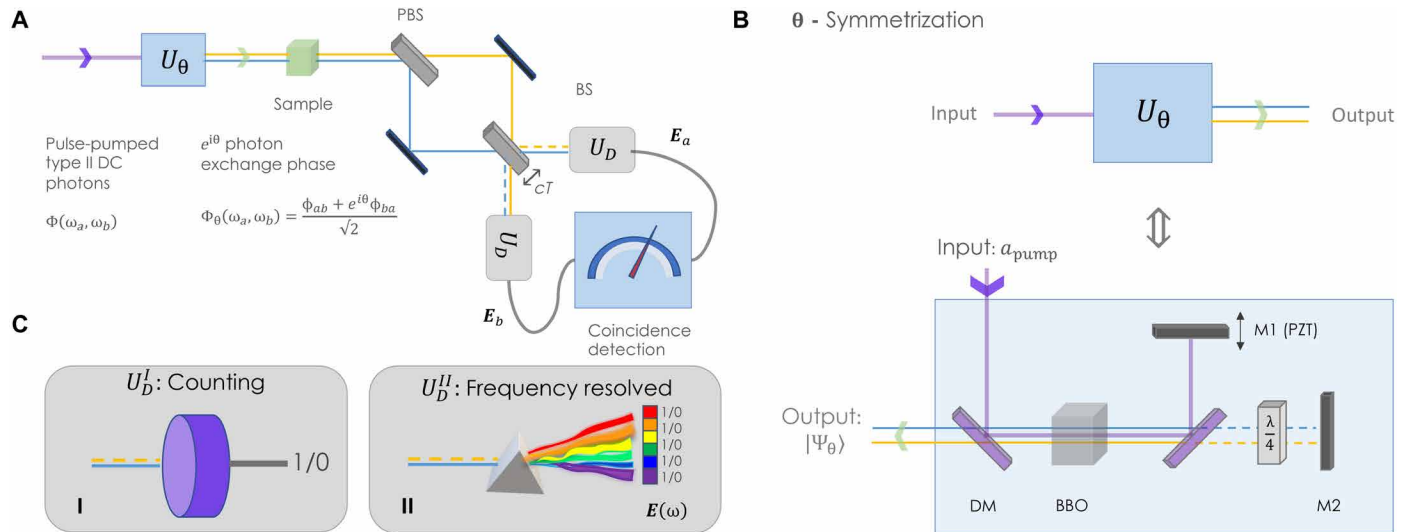


Fig. 1. Multidimensional interferometric spectroscopy setup. (A) Entangled photons with continuously variable exchange phase θ described by U_θ interact with a sample. The pair is separated by a polarization beam splitter (PBS), combined into a Hong-Ou-Mandel (HOM) interferometer, and measured in coincidence following the detection protocol U_D . The HOM setup introduces a relative temporal shift to the photonic pathways, obtained by shifting the BS position $T = \frac{L}{c}$. (B) The θ symmetrization denoted by U_θ is obtained using a modified Michelson interferometer setup. The exchange phase θ grants a varying control over the photon pair degree of distinguishability. (C) Two detection protocols: (I) U_D^I denotes the total photon counting signal (generating a 1/0 event registry), and (II) U_D^{II} denotes the frequency-resolved counting (generating frequency-dependent 1/0 list). M1, mirror 1; M2, mirror 2.

of distinguishability, using the exchange phase engineering described below. At the detection stage, Hong-Ou-Mandel (HOM) interference is sensitive to the post-coupling degree of distinguishability. Symmetric, antisymmetric, and asymmetric optical pathways, each carrying valuable matter information corresponding to different light-matter coupling histories, enable temporal reconstruction. The control parameters available using this setup are summarized at the end of this section.

Preparation

Following (11), a pump beam is directed into a modified Michelson interferometer using a dichroic mirror, as shown in Fig. 1B. The beam passes through a BBO (β -barium borate) crystal, which generates a pair of orthogonally (linearly) polarized entangled photons denoted as signal and idler. The pair is fully characterized by the joint spectral amplitude (JSA) $\phi(\omega_a, \omega_b)$. In our calculations, we have used a JSA given by $\phi(\omega_a, \omega_b) = \mathcal{A}_p(\omega_a + \omega_b)\varphi(\omega_a, \omega_b)$, where $\mathcal{A}_p(\omega) = \exp\left[\frac{-(\omega - \omega_p)^2}{\sigma_p^2}\right]$ is a symmetric pump Gaussian envelope with bandwidth σ_p , centered around the pump frequency ω_p (15). The phase-matching factor $\varphi(\omega_a, \omega_b) = \text{sinc}[(\omega_a - \bar{\omega}_a)T_a + (\omega_b - \bar{\omega}_b)T_b]$ breaks the frequency exchange symmetry. Here, $\bar{\omega}_{a/b}$ are the signal and idler central frequencies, and $T_{a/b} = L(v_{a/b}^{-1} - v_p^{-1})$, where L is the nonlinear crystal length and v is the inverse group velocity at the relevant central frequency ($\bar{\omega}_{a/b}, \omega_p$). The JSA can exhibit strong exchange asymmetry, imprinting the horizontal and the vertical polarization quantum channels with distinct spectral signatures. On one arm, the pump is separated using a dichroic mirror (DM), and its optical path is adjusted equal to the signal and idler (piezo crystal PZT). On the other arm, the polarizations are swapped by passing twice through a $\lambda/4$ plate. In the second passing through the BBO crystal, because of the exchanged polarizations, the spectral profile is flipped from $\phi(\omega_a, \omega_b)$ to $\phi(\omega_b, \omega_a)$ with a relative phase denoted as θ . The

transmitted part of the beam from the DM is finally given by the θ -symmetrized amplitude, resulting in the two-photon wave function

$$|\Psi_\theta\rangle = \int d\omega_a d\omega_b \Phi_\theta(\omega_a, \omega_b) a^\dagger(\omega_a) b^\dagger(\omega_b) |\text{vac}\rangle \quad (1a)$$

$$\Phi_\theta(\omega_a, \omega_b) = \frac{1}{\sqrt{2}} [\phi(\omega_a, \omega_b) + e^{i\theta} \phi(\omega_b, \omega_a)] \quad (1b)$$

where $|\text{vac}\rangle$ is the noninteracting vacuum. Broadband pumping of a type II parametric down converter is known to generate photon pairs with strong spectral distinguishing information (see section S1) (11, 16). We shall show that the asymmetric part of the JSA to (ω_a, ω_b) exchange plays a substantial role in recovering the real part of the matter correlation function for microscopic matter processes that are symmetric to exchange. Figure 2A depicts the nonsymmetrized JSA in frequency domain. Figure 2 (B to D) then present $\theta = \frac{\pi}{2}, 0$, and π used in the cycling protocols presented below. The JSA was computed with $\omega_p = 4$ eV for a 4-mm nonlinear crystal with $T_a = 6.1$ fs and $T_b = 230$ fs. For each value of θ , Fig. 2 (A to D) also presents the Schmidt decomposition in a bar plot of the respective panels. The latter can be interpreted as the probability for the arrival of the n th mode; it provides a measure for the dimensionality of the two-photon Hilbert space and the degree of entanglement (15). Fewer participating modes conform to lower degree of entanglement, while many modes to high degree of entanglement (see Eq. 13 in Materials and Methods). For example, a single mode yields a separable pair, for which measurement of one does not affect the (pure) state of the other. Evidently, the values scanned in Fig. 2 show a relatively low number of participating modes, hence low degree of entanglement. Note that, for $\theta = \pi$, Schmidt modes appear in pairs, as reported in (15, 17).

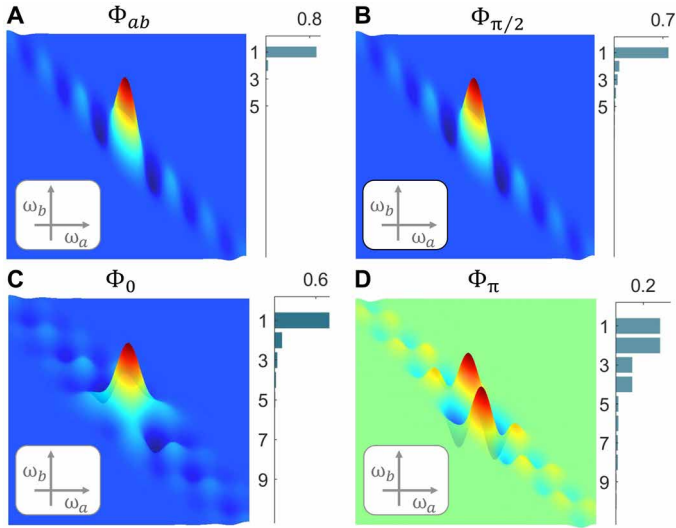


Fig. 2. Joint spectral amplitude. The JSA in Eq. 1b is presented for selection of θ values used on the exciton model system. (A) The nonsymmetrized amplitude two-photon amplitude in frequency domain, with Schmidt number $\kappa = 1.01$. Symmetrized amplitude using (B) $\theta = \frac{\pi}{2}$ with $\kappa_s = 1.06$, (C) $\theta = 0$ with $\kappa_0 = 1.58$, and (D) antisymmetric $\theta = \pi$ with $\kappa_\pi = 2.87$. Each bar plots signifies the Schmidt decomposition resulting from the corresponding amplitude.

Detection and coupling

The coincidence signal is obtained by a two-photon expectation value at the detection plane. Since a detection event involves an annihilation of a photon by the detector, we begin our analysis from the detection stage. We then describe the light-matter interaction stage using the joint photon-sample density operator. Interferometric setups can be described by a linear transformation of the field modes between the detection and interaction stages (3). Two coincidence detection protocols are considered as depicted in Fig. 1. The corresponding coincidence observables U_D^I and U_D^{II} reflect two-photon populations in their respective (time frequency) domain. Both setups contain several independent control parameters that manipulate the excitation and detection mechanisms. Detection-related control parameters include the HOM relative delay T , and, when resolved (U_D^I), the detected frequencies (ω_a, ω_b). The excitation-related control parameters are the exchange phase θ , pump bandwidth σ_p , pump central frequency ω_p , and the pair central frequencies ($\bar{\omega}_a, \bar{\omega}_b$). The first three parameters ($\theta, \sigma_p, \omega_p$) can be scanned continuously in a single setup. The entangled pair central frequencies ($\bar{\omega}_a, \bar{\omega}_b$) are additional control parameters, which require a special extended phase-matching preparation (18).

Total coincidence signal – U_D^I

The total coincidence count is described by a photon annihilation of two modes at the two detectors. When the signal is not resolved temporally, the annihilation time is integrated over and the corresponding observable is given by the operator

$$\widehat{\mathcal{O}}_I(t_a, t_b) = E_{a,R}^\dagger(\mathbf{r}_a, t_a) E_{b,R}^\dagger(\mathbf{r}_b, t_b) E_{b,L}(\mathbf{r}_b, t_b) E_{a,L}(\mathbf{r}_a, t_a) \quad (2)$$

Here, E_R and E_L are electric field superoperators, corresponding to Hilbert space operators, that act from the right $E_{RP} \equiv \rho E$ and left

$E_{LP} \equiv E \rho$ of the density operator. The Hilbert space polarization-dependent field operator is given by $E_\sigma(\mathbf{r}, t) = \sum_{\mathbf{k}} \sqrt{\frac{2\pi\hbar}{\Omega_Q}} \hat{\mathbf{e}}_\sigma(\mathbf{k}) a_{\mathbf{k},\sigma}(t) e^{i\mathbf{k}\cdot\mathbf{r}}$, where $\hat{\mathbf{e}}_\sigma(\mathbf{k})$ is the σ -polarization vector, Ω_Q is the quantization volume ($c = 1$), and $a_{\mathbf{k},\sigma}(a_{\mathbf{k},\sigma}^\dagger)$ are annihilation (creation) operators obeying the bosonic commutation relations $[a_{\mathbf{k},\sigma}, a_{\mathbf{k}',\sigma'}^\dagger] = \delta_{\sigma,\sigma'} \delta_{\mathbf{k},\mathbf{k}'}$. $\widehat{\mathcal{O}}_I$ represents the photon detection as annihilation of two modes from the left and right of the density operator, projecting the two-photon subspace in the measurement. The coincidence signal is obtained by taking the expectation value of Eq. 2 in the interaction picture

$$\mathcal{C}[\Lambda_I] = \int dt_a dt_b \left\langle \mathcal{T} \widehat{\mathcal{O}}_I(t_a, t_b) \exp \left\{ -\frac{i}{\hbar} \int_{t_0}^t ds H_{\text{int},-}(s) \right\} \right\rangle \quad (3)$$

where $\Lambda_I = \{\omega_p, \sigma_p, \theta, T\}$ represents the set of control parameters available in this measurement protocol. $\langle \widehat{\mathcal{O}} \rangle \equiv \text{tr} \{ \widehat{\mathcal{O}} \rho_0 \}$ denotes the trace with respect to the initial state of the joint density operator $\rho_0 = \rho(t_0)$, and \mathcal{T} is the time-ordering superoperator. The light-matter coupling is described by the interaction superoperator corresponding to the commutator of the Hilbert space interaction Hamiltonian and the density operator, $H_{\text{int},-} \rho \equiv [H_{\text{int}}, \rho]$. We adopt the multipolar interaction Hamiltonian in the rotating wave approximation (RWA) $H_{\text{int}} = E^\dagger \cdot V + H.c.$, where V is the dipole-lowering operator. Within the RWA, emission (absorption) of a photon is associated with energy decrease (increase) of the sample. The total coincidence counting signal \mathcal{C}_I is obtained by integration over photon arrival times, unresolved due to the absence of temporal gating.

The frequency-resolved coincidence counting – U_D^{II}
The frequency-resolved signal is obtained by a double annihilation of photons and is defined by the corresponding frequency-domain superoperators. These are related to time-domain counterparts using Fourier transform $E_\sigma(\mathbf{r}, t) = \int \frac{d\omega}{2\pi} e^{i\omega t} E_\sigma(\mathbf{r}, \omega)$. Similarly, the observable $\widehat{\mathcal{O}}_{II}$ is given by

$$\widehat{\mathcal{O}}_{II}(\omega_a, \omega_b) = E_{a,R}^\dagger(\mathbf{r}_a, \omega_a) E_{b,R}^\dagger(\mathbf{r}_b, \omega_b) E_{b,L}(\mathbf{r}_b, \omega_b) E_{a,L}(\mathbf{r}_a, \omega_a) \quad (4)$$

and the coincidence signal is obtained by the respective expectation value

$$\mathcal{C}[\Lambda_{II}] = \left\langle \mathcal{T} \widehat{\mathcal{O}}_{II}(\omega_a, \omega_b) \exp \left\{ -\frac{i}{\hbar} \int_{t_0}^t ds H_{\text{int},-}(s) \right\} \right\rangle \quad (5)$$

Here, $\Lambda_{II} = \{\omega_a, \omega_b, \omega_p, \sigma_p, \theta, T\}$ are the corresponding control parameters.

When implementing Eqs. 3 and 5, it is crucial to note that the light-matter coupling takes place at different stages of the interferometer. Consequently, they are defined in different basis sets and require the linear transformation, as described below.

Interferometric photon basis-transformation

Because of the HOM interferometer, the optical modes involved in the light-matter coupling and the detected modes are given in different basis sets. The transformation (Jordan-Schwinger map) can be represented using an $SU(2)$ rotation in the frequency domain (19–23), resulting in the input-output relation

$$\widehat{\mathcal{R}}_T = \begin{pmatrix} t & ire^{i\omega T} \\ ire^{-i\omega T} & t \end{pmatrix} \quad (6)$$

used in the derivation of the signal. Here, t and r are the transmission and reflection coefficients obeying $|t|^2 + |r|^2 = 1$, and T is the relative time delay. For the 50:50 beam-splitter (BS) considered here, $t = r = 1/\sqrt{2}$. The field in vector notation is given by $\mathbf{E}(\mathbf{r}, \omega) = (E_a(\mathbf{r}, \omega), E_b(\mathbf{r}, \omega))^T$. Under the HOM rotation, the detected field is given by $\mathbf{E}|_{\text{detection}}(\mathbf{r}, \omega) = \hat{\mathcal{R}}_T \mathbf{E}|_{\text{interaction}}(\mathbf{r}, \omega)$. In the following, we express all field operators in the interaction domain basis $\mathbf{E}|_{\text{interaction}} \equiv \mathbf{E}(\mathbf{r}, \omega)$, which requires the inverse rotation of the observable in Eq. 2 (see the Supplementary Materials for detailed derivation) (3).

Application to an exciton model system

We consider the three-level model system depicted in Fig. 3A with energy manifolds (g, e, f) corresponding to the ground, singly, and doubly excited states, respectively. To resemble four WM (4-WM), we expand Eqs. 3 and 5 to fourth-order light-matter coupling H_{int} . In Fig. 3B, we show two groups of light-matter pathways: two-photon resonance (TPR) represented by diagram D_1 and Raman processes (RP) (diagrams D_2 and D_3). The TPR pathways begin with a two-photon absorption event $|\{g\}\rangle \rightarrow |\{e\}\rangle \rightarrow |\{f\}\rangle$, while RPs solely represent $|\{g\}\rangle \leftrightarrow |\{e\}\rangle$ transitions and do not involve

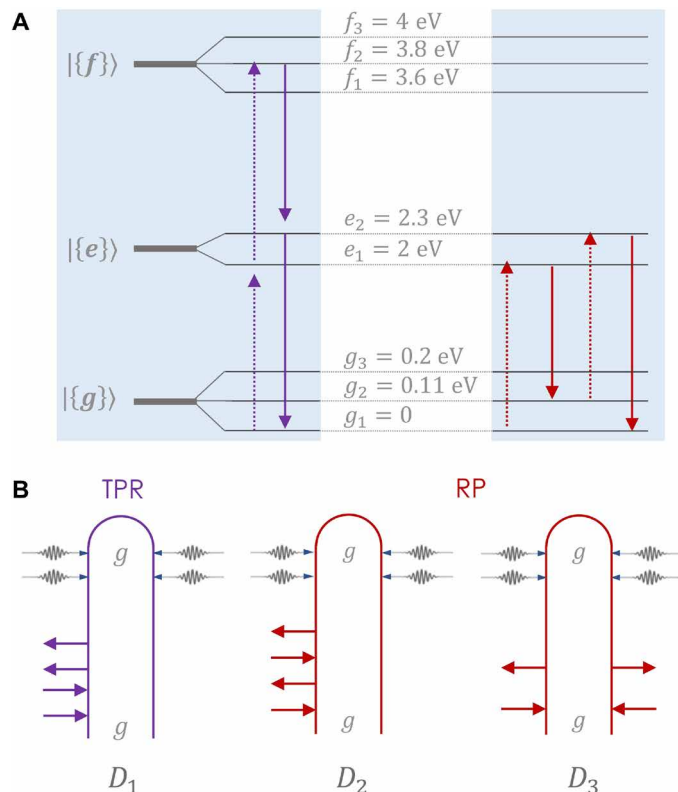


Fig. 3. Exciton model system and coupling pathways. (A) Three-level model system composed of ground $|\{g\}\rangle$, single $|\{e\}\rangle$, and doubly excited $|\{f\}\rangle$ manifolds. The red arrows pointing interchangeably up and down correspond to Raman pathways. The purple arrows arranged in two consecutive absorptions followed by two emissions correspond to TPRs. (B) Diagrammatic representation of the contributing microscopic light-matter processes. Straight arrows represent an interaction corresponding to both fields. Curved arrows represent the detection (annihilation) process. Diagram D_1 involves double excitations (reaching the f manifold) and referred to as TPR. D_2 and D_3 describe single excitations (e manifold) and denoted RP. The two distinct subgroups of processes are depicted in (A).

the f manifold. The diagrams describe the light-matter interaction on a closed-time (Keldysh) contour in which the ket (bra) evolve forward (backward) in time (24, 25). The sample is taken to be initially in the ground-state $\rho_\mu(-\infty) = |g_1\rangle\langle g_1|$. Each inward (outward) arrow denotes interaction-induced excitation (de-excitation) of the sample, and the final state of the sample is stated at the top of each diagram. Note that reflection (interchanging the bra-ket arrows) of all D_i results in complex conjugation. We assume an initially uncorrelated field-matter density operator $\rho(-\infty) = \rho_\varphi(-\infty) \otimes \rho_\mu(-\infty)$, where $\rho_\varphi(-\infty) = |\Psi_\theta\rangle\langle\Psi_\theta|$ is the two-photon initial pure state.

Below, we present the signals obtained using the two coincidence-counting detection protocols presented in Fig. 1, U_D^{HOM} . The probability of observing each pathway (D_i) varies with the number of detected photons and is therefore sensitive to the final state of the sample, in contrast to signals obtained with a classical source. When single photons are detected, all processes contribute regardless to the number of generated photons (26, 27).

Total coincidence

The celebrated HOM dip is a minimum in the total coincidence count of photon pairs, obtained upon changing the degree of their distinguishability by varying their relative path delay T (28). The signal attains its minimal value for $T = 0$ and vanishes altogether when the pair is completely indistinguishable. The U_D^{HOM} detection protocol manifests a HOM interference of the pair, posterior to the interaction with the sample. Matter energy fluctuations shape the interference pattern of the applied field and then recorded as the signal.

The coincidence signal eq. S7 is derived using diagrams D_1 , D_2 , and D_3 for general pulse parameters and the corresponding symmetrization procedure (initial state) in section S1. Simplified expressions are obtained for a narrowband pump pulse with frequency-degenerate entangled pair, fixing $\omega_a = \omega_b = \omega/2$. This is possible by adopting phase-matching condition $\varphi(\omega_a, \omega_b)$, which is maximal for identical central frequencies $\bar{\omega}_a = \bar{\omega}_b$ of the entangled pair. We assume a narrowband pump of bandwidth (full width at half maximum) $\Delta\lambda/\lambda_p \leq 10^{-2}$, where λ_p is the central frequency of the pump. The central frequency is scanned in the 0.1- to 3-eV regime attainable by pulse duration $\tau_p \approx 0.1$ to 10 ps for a transform-limited Gaussian pulse. Combined with the degenerate phase-matching factor, the signal is maximal for $\omega_a = \omega_b = \omega/2$. Under these conditions, it is possible to isolate the contribution of diagram D_3 and probe the intraband dephasing in real time. This measurement requires no time-resolved detection and is exclusively based on the HOM relative delay, which is not conjugate to any frequency variable. The total coincidence signal (eq. S7) then reduces to

$$\begin{aligned} \mathcal{C}[\Lambda_I] &= \mathcal{C}\left[\omega_p \frac{\sigma_p}{\omega_p} \ll 1, \theta = 0, T\right] \\ &\propto \Re \text{tr} \left\{ \text{VG}^\dagger \left(\frac{\omega_p}{2} \right) \text{V}^\dagger [1 - iG(T)] \text{VG} \left(\frac{\omega_p}{2} \right) \text{V}^\dagger \rho_\mu(-\infty) \right\} \end{aligned} \quad (7)$$

where we have used the fully symmetric initial state for the field ($\theta = 0$), selectively isolating D_3 . Here, $G(t) = -i\theta(t) e^{-iH_\mu t}$ is the Green function of the sample and its Fourier transform $G(\omega) = 1/(\omega - H_\mu + i\gamma)$, introducing a phenomenological dephasing rate γ ($\hbar = 1$). It is convenient to interpret Eq. 7 using the density matrix: the sample optically pumped to an excited state population and then

de-excited back to the ground manifold, where the observable $1 - iG(T)$ is measured (see eq. S9 for the sum-over-states expression). The time domain Green's function is evaluated at the $|\{g\}\rangle$ manifold, revealing its temporal dynamics at time T . Scanning ω_p and performing the Fourier transform of the signal with respect to the pair $\{\omega_p, T\}$, we obtain the two-dimensional (2D) signal depicted in Fig. 4A from Eq. 7. Note that T and ω_p are nonconjugate variables and can be jointly resolved to arbitrary accuracy. The spectral-temporal information in Fig. 4A can be reduced to a single dimension (time or frequency) in multiple ways. One way to achieve that is by tracing uniformly ω_p , keeping the HOM delay T

$$C_T = \int \frac{d\omega_p}{2\pi} C[\Lambda_I] \tag{8}$$

as depicted in Fig. 4B. The exponential decay envelope of the intraband dephasing is clearly visible along the variation of T . Two dephasing rates are illustrated $\gamma_g = 1$ meV and 2 meV, as well as the fast decay of γ_{eg} . The temporal resolution of the intraband dephasing is determined solely by the HOM delay (T) step size. The signal peaks notably when $\omega_{p/2}$ is resonant with the interband transitions $\omega_{e_i g_j}$ within the frequency scanning range. This can be rationalized by the sum-over-states expression of Eq. 14.

To extract spectral information, it is convenient to look at cross sections of a given time delay. We find maximal contrast in the spectral features for almost vanishing delays $T = 0^+$. We denote this cross section

$$C_{\perp} \equiv C\left[\omega_p, \frac{\sigma_p}{\omega_p} \ll 1, \theta = 0, T = 0^+\right] \tag{9}$$

in Fig. 4 (C and D). Figure 4C depicts the spectrum obtained for $\gamma_g = 1$ meV (4 ps) and more rapid interband dephasing $\gamma_{eg} = 10$ meV (0.4 ps) in logarithmic scale. Figure 4B presents the same for equal interband and intraband dephasing $\gamma_{eg} = \gamma_g = 1$ meV (4 ps). The lineshapes are broadened because of the properties of the sample. We thus infer that rapid γ_{eg} decay is a limiting factor in the spectral resolution of the interband transitions in this detection scheme.

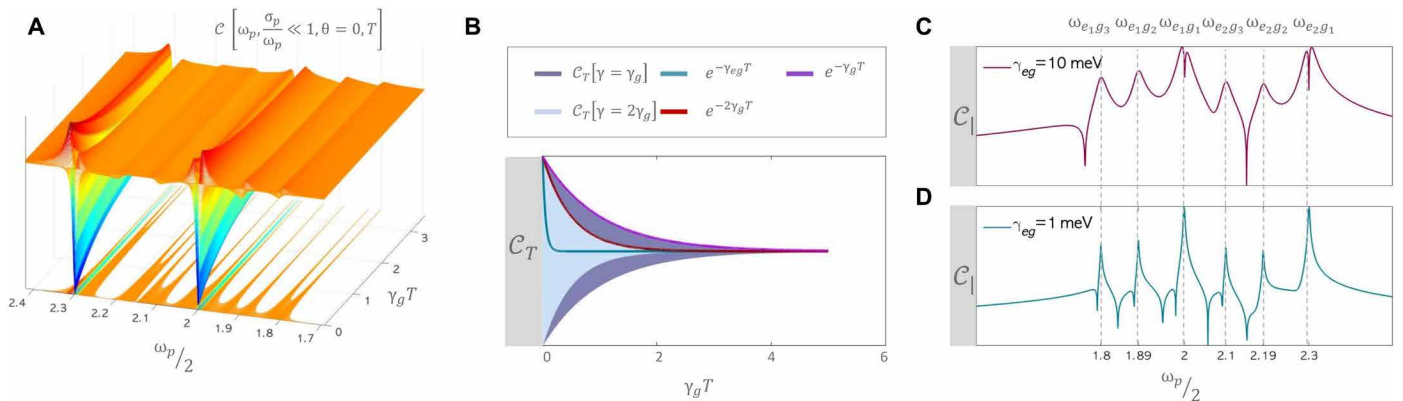


Fig. 4. Coincidence counting of the exciton system. (A) The total coincidence-counting 2D signal (U_D^I detection protocol) with respect to the HOM delay T and the pump central frequency $\omega_{p/2}$ obtained from Eq. 7. The signal is obtained by a narrowband frequency-degenerate photon pair, corresponding to the intraband dephasing rate $\gamma_g = 1$ meV (4 ps). (B) Illustration of Eq. 8: The total coincidence-counting signal as a function of the HOM delay for two chosen dephasing rates $\gamma_g = 1$ meV and $2\gamma_g$ and the respective exponential envelopes integrated over the pump frequency. The interband spectrum obtained from Eq. 9 is displayed for two interband transition rates in (C) $\gamma_{eg} = 10$ meV and (D) $\gamma_{eg} = 1$ meV.

Frequency-resolved coincidence

A natural extension of the total coincidence counting is provided by frequency-resolved photon detection (protocol U_D^{II} in Fig. 1). This adds two control parameters to the above signal, resulting in the following set of control parameters $\Lambda_{II} = \{\omega_a, \omega_b, \theta, T, \omega_p, \sigma_p\}$. Expansion of Eq. 5 to fourth order in H_{int} introduces an additional phase factor $\exp\{i\eta\}$ associated with the HOM delayed path trajectories, where $\eta = (\omega_a - \omega_b)T$ (see section S3 for detailed derivation). There are many ways to display the resulting high-dimensional signal. We use the shorthand notation $C_\theta(\eta) \equiv C[\Lambda_{II}]$, where η can be fixed for any pair of frequencies (ω_a, ω_b) using the delay variable T . It is convenient to introduce the auxiliary functions corresponding to the real $\mathcal{R}_i \equiv \Re\{\Xi_i\}$ and imaginary $\mathcal{I}_i \equiv \Im\{\Xi_i\}$ parts of the respective pathway contributions. Here, $i = \{\text{TPR, RP}\}$ and Ξ_i encapsulate all microscopic processes that contribute to each pathway (see section S3 for the full expressions). The choice $(\theta, \eta) = (0, \pi)$ gives

$$C_0(\pi) = \mathcal{I}_{\text{TPR}}(\omega_a, \omega_b) + \mathcal{I}_{\text{RP}}(\omega_a, \omega_b) \tag{10}$$

where both groups of pathway are observed, as shown in Fig. 5A. In our calculations, we have used an entangled pair generated by a broadband pump with $\sigma_p = 0.9$ eV (≈ 1 -fs pulse). The central frequency ω_p is scanned in the range of 2 to 5 eV, and all dephasing rates are identical $\gamma_{ij} = 5$ meV. To quantify the degree of entanglement generated by the two-photon source, we compute the Schmidt number $\kappa_\theta \equiv [\sum_n p^2(n|\theta)]^{-1}$ (see Materials and Methods). The Schmidt number for the above parameters is $\kappa_0 \approx 2.7$, using nonlinear crystal of length $L = 0.4$ mm. Figure 5A depicts all contributing pathways, where we observe distinct TPR features located along the diagonal lines in which $\omega_a + \omega_b = \omega_{f_i g_j}$ such that $\omega_{a/b} = \omega_{e_i g_1}$ $\omega_{b/a} = \omega_{f_i e_j}$. The RP pathways are observed along the lines corresponding to the transitions $\omega_{e_i g_j}$. Similar results are obtained with doubled bandwidth (σ_p) corresponding to $\kappa_0 \approx 1.7$. The coincidence signal vanishes for $(\theta, \eta) = (0, 0)$ as expected for indistinguishable photons. For presentation purposes, all images in Fig. 5 are displayed by sweeping and summing the pump central frequency ω_p . In movies S1

Downloaded from https://www.science.org at University of California Irvine on September 23, 2021

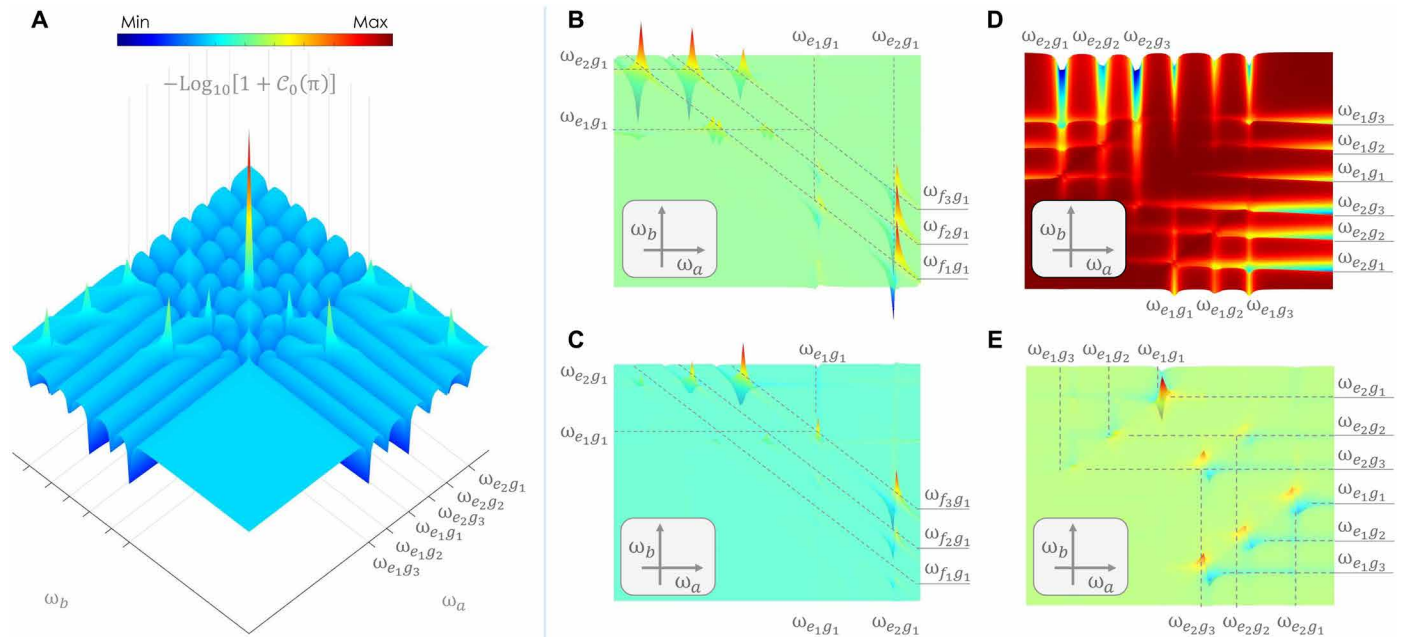


Fig. 5. Frequency resolution of the exciton signal and exchange-phase cycling. (A) 2D spectra obtained from Eq. 10 using ultrafast pump with $\sigma_p = 0.9$ meV and scanning ω_p in the range of 2 to 5 eV on logarithmic scale. The exchange-phase cycling protocol shows each of the components selectively. The imaginary (B) and real (C) part of the TPR pathway given by the cycling protocols in Eqs. 11a and 11b, respectively. The dashed diagonal lines follow the doubly excited transition $\omega_a + \omega_b = \omega_{fg}$. The imaginary (D) and real (E) part of the RP pathway following the cycling protocols in Eqs. 11c and 11d. The dashed lines denote transitions between the first excited and ground manifolds $\omega_{e,g}$.

and S2 (see Materials and Methods for more information), this protocol is shown to maintain the desired spectral information.

Exchange-phase cycling

Pathway selectivity can help in studying the molecular dynamics in greater detail. Frequency-resolved detection (U_D^H) depicted in Fig. 1 achieves just that: isolating the real and imaginary part of various diagrams exclusively.

We propose exchange-phase cycling protocols, whereby several signals obtained with different control parameters are combined to selectively probe desired pathways. These exploit the Michelson and the HOM interferometers to manipulate the effective exchange phases before and after the interaction, respectively (θ , η). The Michelson interferometer (Fig. 1B) imprints any permutation of the initial photon pair with a relative phase factor. The HOM detection interferometer introduces path-related phase factor to the detected photons. Certain combinations of (θ , η) are useful for reconstructing the real and imaginary parts of the signals individually (see section S3 for derivation and final expressions). It is useful to examine the Fourier transform of the coincidence signal $\mathcal{D}_\theta = \int dT e^{-i\Omega T} \mathcal{C}_\theta(\eta)$ (presenting 2D spectral map along the lines $\Omega = \omega_a - \omega_b$). Combinations of $\mathcal{C}_\theta(\eta)$ and \mathcal{D}_θ allow the phase-sensitive reconstruction of the TPR and RP processes.

There are multiple choices of linearly dependent cycling protocols to achieve path selectivity. Here, we display one cycling protocol resulting in the 2D spectra presented in Fig. 5 (A to E). The information displayed in Fig. 5 (B-E) depict the cycling protocol below corresponding to the real \mathcal{R}_i and imaginary \mathcal{I}_i parts of the respective contribution

$$\mathcal{I}_{\text{TPR}}(\omega_a, \omega_b) = C_\pi(\pi) \quad (11a)$$

$$\begin{aligned} \mathcal{R}_{\text{TPR}}(\omega_a, \omega_b) &= D_{\frac{\pi}{2}} - D_{-\frac{\pi}{2}} - C_{\frac{\pi}{2}}(0) + C_{-\frac{\pi}{2}}(0) \\ &+ C_{\frac{\pi}{2}}\left(\frac{\pi}{2}\right) - C_{-\frac{\pi}{2}}\left(\frac{\pi}{2}\right) \end{aligned} \quad (11b)$$

$$\mathcal{I}_{\text{RP}}(\omega_a, \omega_b) = D_{\frac{\pi}{2}}(0) + C_{-\frac{\pi}{2}}(0) \quad (11c)$$

$$\mathcal{R}_{\text{RP}}(\omega_a, \omega_b) = C_{\frac{\pi}{2}}(0) - C_{-\frac{\pi}{2}}(0) \quad (11d)$$

In the following calculations, we have used an entangled pair generated by a pump with varying bandwidth: from a narrowband $\sigma_p = 1.8$ meV corresponding to ≈ 1 -ps pulse to broadband $\sigma_p = 0.9$ eV using a ≈ 1 -fs pulse. The central frequency ω_p is scanned in the 2- to 5-eV regime, and all dephasing rates are identical $\gamma_{ij} = 5$ meV. The real part of the response is strongly dependent on the degree of asymmetry of the initial state wave function. The asymmetric part of the JSA becomes more pronounced in the broadband regime and is negligible for a narrowband pulse (11, 29). The signals corresponding to the protocols in Eqs. 11a to 11d were calculated using an ultrafast pump with $\sigma_p = 0.9$ eV and are depicted in Fig. 5 (B to E), respectively. The Schmidt number κ_θ (Eq. 13) for the above parameters and a $L = 0.4$ mm varies between 1 and 5 (depending on θ). Figure 5 (B and C) presents the TPR pathways, where we observe dispersive features (30) located along the diagonal lines in which $\omega_a + \omega_b = \omega_{fg}$ such that $\omega_{a/b} = \omega_{e/g_1}$ and $\omega_{b/a} = \omega_{f/e_1}$. Note that the transition $\omega_{f_3e_1} = \omega_{e_1g_1} = 2$ eV is not resolved in \mathcal{I}_{TPR} , yet it appears in \mathcal{R}_{TPR} ; this

stems from the antisymmetric nature of the JSA $\Phi_{\pi}(\omega_a, \omega_b)$, which vanishes when $\omega_a = \omega_b$. While \mathcal{I}_{TPR} is symmetric to the exchange, \mathcal{R}_{TPR} is antisymmetric and thus fully resolved. Nonetheless, different choices of cycling protocols may resolve this transition (see Fig. 5A and section S5 for such example). Figure 5 (D and E) depicts the RP pathway, scanning the single exciton manifold from which all transitions ω_{egj} are visible. Last, one can verify that the information in Fig. 5A displays a combination of Fig. 5 (B and D), excluding the degenerate transitions in which $\omega_a = \omega_b$.

Comparison with ordinary WM

Nonlinear spectroscopic signals are usually described semiclassically using a sequence of temporally separated bright classical pulses (containing many photons) that trigger matter dynamics and generate a single photon (14). This photon is modulated by m light-matter interactions, resulting in an $m + 1$ order correlation function. Nonlinear $m + 1$ WM is given by the expectation value of the integrated change of the electric field intensity $I = \int dt \langle \dot{\mathcal{I}} \rangle$ (31). The intensity is a single-photon quantity, related to the electric field operator $\mathcal{I} = \mathbf{E}^\dagger \mathbf{E}$. Quantum sources can achieve superior signal-to-noise ratio scaling with the number of photons. This superior scaling is referred to as the Heisenberg limit in quantum metrology (32–36), enabling reduced radiation exposure for comparable measurement certainty. Particularly, the offer to improve the resolution of fragile samples, limited by radiation dose constraints (37). One way to benefit from the quantum properties of the electromagnetic field is via direct coupling of quantum light to the sample (e.g., entangled photons and squeezed states). Sample stimuli using quantum sources have shown to yield remarkable control over population dynamics and pathway selection (26, 38, 39). Alternatively, as done here, one can probe quantum effects of the emitted radiation directly via multiple photon counting [e.g., antibunching (40) and superresolved imaging (41–44)].

Multiple photon detection yields higher-order WM signals, denoted $(n + m)$ -WM in analogy to the semiclassical $(m + 1)$ -WM. It involves the application of m fields and the detection of n -generated photons that give rise to $n + m$ order correlation function. While $(m + 1)$ -WM depend on several pathways, $(n + m)$ -WM contain fewer terms and may not be written in the form of amplitude square. In our setup, coincidence counting eliminates the single-photon diagram depicted in Fig. 6 denoted S, since only one photon is populated in the final state. This yields substantial change compared to single-photon (intensity) signal. Semiclassical nonlinear WM signals are generated from nonlinearities in matter (12, 13). Thus, collective excitations in the f manifold with energies $\epsilon_{fkg} = \epsilon_{eig} + \epsilon_{ekg}$ vanish. This stems from the fact that the last light-matter interaction in D_1 (Fig. 3) propagates forward in time (applied to the ket), while, with S in Fig. 6, backward in time (applied to the bra). Therefore, for small dephasing rates, the forward and backward resonances inherit opposite relative sign, verified using the Sokhotski-Plemelj theorem $\lim_{\gamma \rightarrow 0} \frac{1}{\omega \pm i\gamma} = \mp i\pi\delta(\omega) + \text{pp}(\frac{1}{\omega})$, where pp denotes the principle part. Because of the elimination of S, the coincidence signal here is sensitive to collective excitations in TPR processes.

$(n + m)$ -WM also gives rise to different scaling with the pulse intensity. For example, double excitation signals induced by entangled pairs are known to scale linearly (rather than quadratically) with the pump intensity $\propto I_p$ (45–47). This permits the study of doubly excited manifold with smaller probability of ground-state bleaching, thus potentially reduce sample damage. While single-photon detection events scale linearly with the pump intensity $\propto I_p$, the two-photon

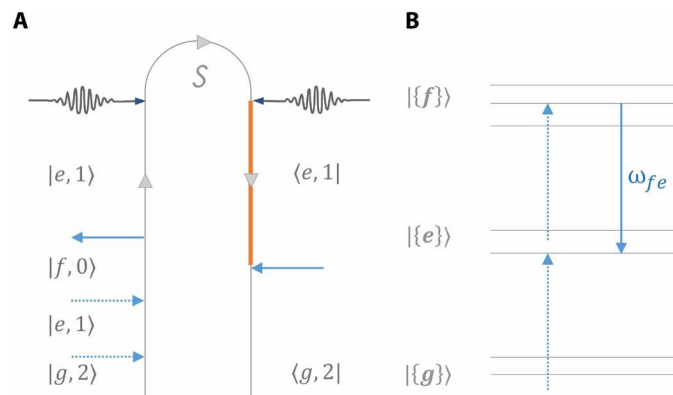


Fig. 6. TPR process missing in the coincidence signal. (A) A single-photon TPR process labeled S, which involve double excitations (f manifold). The joint field matter is specified after each interaction event on the diagram. The highlighted (orange) line corresponds to the backward propagator responsible for the elimination of the (harmonic) collective excitations in single-photon nonlinear signals. (B) Schematic representation of the process.

signal scales quadratically $\propto I_p^2$. This allows using lower intensities per desired detection gain, improving signal-to-noise ratio (48–50). This principle can be extended to n photon population detection in a straightforward manner.

DISCUSSION

The measurement of a specific number of photons using coincidence detection narrows down the observed dynamical pathways of the observed process. Pathways that the sample ends up in a certain final state are sorted out. In contrast, WM signals obtained with classical light probe a coherence and are not sensitive to the final state of the sample. Specifically, two-photon coincidence of a pair, which is weakly coupled to a sample, generates a unique $(2 + 2)$ WM that probes a limited number of pathways. Similar to 4-WM, the signal considered here depends on a four-point dipole correlation function of matter. The difference is that the elaborate detection does not single out one field, as in semiclassical 4-WM signals, but two fields are detected. We can thus view the process as a generalized 4-WM. To avoid confusion, we simply refer to it as $(2 + 2)$ WM, which specifies the number of applied and detected fields.

Our first detection scheme records the total photon coincidence count without any spectral and temporal resolutions. The two-natural control parameters of the setup depicted in Fig. 1 are the HOM delay T and the central frequency of the pair-generating pump ω_p . A remarkable effect occurs with the application of a degenerate photon pair [extended phase-matching condition (51, 52)] with a symmetric narrowband JSA ($\theta = 0$), such that both photons are sharply distributed around half the pump frequency $\frac{\omega_p}{2}$. The TPR pathways are then eliminated, and only a single RP pathway (D_3 ; Fig. 3) survives. The following dynamics is then observed: (i) The density matrix of the sample is excited and then de-excited back to the initial band $|\{g\}\rangle$. (ii) The Green function of the system at time T is measured. Since T is controlled with high precision, the intraband dephasing dynamics can be reconstructed in real time as shown in Fig. 4 (A to D). This allows to characterize the system's coupling to its environment. Small T expansion $\langle H^n \rangle$ and is given in section S2. This provides a compelling direction for

future study aligned with the efforts invested in studying decoherence and energy leaks in quantum technologies.

Our second detection protocol involves frequency-resolve coincidence counting. By cycling values of T and the entangled pair exchange phase θ , we can separate the TPR and RP pathways. Pathway-selection protocols typically generate destructive interference to suppress certain populations (26) or induce distinct scaling of each process with the intensity (38). Here, pathways are selected by projecting the high-dimensional signal to process-specific data, without reducing the event probability of other processes. Moreover, by combining signals with different θ and $T(\omega_a - \omega_b)$ (phase cycling), we can obtain the phase of four-point matter correlation function, as shown in Fig. 5 (B to E). Temporal reconstruction is then possible using a simple Fourier transform. The cycling protocols related to the real part of the correlator require an asymmetric JSA with respect to exchange, inherited from the ultrafast pump. This suggests that obtaining temporal behavior of the correlators necessitates an ultrashort generating pump, which is compatible with temporal resolution, although this is a frequency domain measurement. An ultrashort pump generates a spontaneous photon pair that carries an identity-revealing spectral information (16). The resulting distinguishability renders a “which pathway?” information available. The relation between the JSA asymmetry and the temporal resolution upper-bound warrants a further study, since the temporal and spectral control parameters are not conjugate quantities. These effects are more pronounced at low entanglement values and steered by the variable effective exchange phase.

In addition to the above merits, matter-induced field nonlinearities may also improve the frequency resolution (35, 36). Correlation-based detection techniques (e.g., coincidence) can reveal such electromagnetic field nonlinearities. These correlations have signatures in matter-induced photon-photon coupling (53), free-electrons coupling (54), and thus carry matter information that is imprinted in the postinteraction counting statistics. Characterization of the reading process that can access this information is one of the central goals of interferometric spectroscopy.

MATERIALS AND METHODS

Schmidt number calculation

The Schmidt number is a measure of photon entanglement that depends on the single photon density matrix. It is based on the Schmidt decomposition of the JSA (15)

$$\Phi_{\theta}(\omega_a, \omega_b) = \sum_n \sqrt{p(n|\theta)} \psi_n(\omega_a) \phi_n(\omega_b) \quad (12)$$

Here, $\{\psi_n, \phi_n\}$ are an eigenfunctions of the single-photon reduced density matrix and $p(n|\theta)$ are their weights. To obtain this representation, we solve $p(n|\theta)\psi_n(\omega) = \int d\omega' K_1(\omega, \omega')\psi_n(\omega')$ and $p(n|\theta)\phi_n(\omega) = \int d\omega' K_2(\omega, \omega')\phi_n(\omega')$. These kernels are found from the reductions $K_1(\omega, \omega') = \int d\omega'' \Phi_{\theta}(\omega, \omega'') \Phi_{\theta}^*(\omega', \omega'')$, tracing the second frequency variable, and $K_2(\omega, \omega') = \int d\omega'' \Phi_{\theta}(\omega'', \omega) \Phi_{\theta}^*(\omega'', \omega')$. They can be interpreted as single-photon correlation functions. The Schmidt decomposition computed by a diagonalization of the discretized single-photon reduced density matrix, following the procedure in (15). Here, $p(n|\theta)$ can be interpreted as the n th mode probability using θ -symmetrized JSA. It provides a measure for the effective two-photon Hilbert space. To obtain the Schmidt spectrum and characterize the degree of entanglement, we discretize the

kernels and numerically solve the integral eigenvalue equations. We have used a 900 by 900 grid for the discretized kernel and calculated separately for each θ . The Schmidt number (also known as the participation ratio) is obtained by

$$\kappa_{\theta} \equiv \frac{1}{\sum_n p^2(n|\theta)} \quad (13)$$

it is a measure of the number of relevant Schmidt modes.

Intraband dephasing signal computation

Equation 7 reveals the intraband dephasing in the time domain by scanning the HOM relative delay T . We express the correlation functions using the dipole-lowering operator $V = \sum_{i>j} \mu_{ij} |j\rangle\langle i|$ and its complex conjugate, where (i, j) label energy eigenstates of the exciton system corresponding to $|g_i\rangle$, $|e_i\rangle$, and $|f_i\rangle$. The expectation value in Eq. 7 requires Green's function of the sample in frequency domain $G(\omega) = (\omega - H + i\gamma)^{-1}$, where H is the Hamiltonian of the sample. With these definitions, we obtain the coincidence counting for our model system

$$C[\Lambda_j] \propto \Re e \sum_{e, e', g'} \frac{1}{\frac{\omega_p}{2} - \omega_{e'g'} - i\gamma_{e'g'}} \frac{1}{\frac{\omega_p}{2} - \omega_{eg} + i\gamma_{eg}} \langle g' | [1 - iG(T)] | g' \rangle \quad (14)$$

used in the calculations presented in Fig. 4. The short-lived excited states of the first excited manifold serve as a prefactor to the relaxation process of the ground-state manifold. The calculation of Eq. 14 in Fig. 4 was carried out on a discretized grid by scanning 10^4 frequency and 10^3 points corresponding to ω_p and T , respectively.

2D spectra calculations

The results for the frequency-resolved coincidence section were obtained by direct implementation of eqs. S22 to S25 in section S4. The JSA was discretized within the shown interval in Fig. 5 in a $200 \times 200 \times 200$ corresponding to ω_a , ω_b , ω_p , and T for the implementation of the numerical integration. The signal shown in Fig. 5 is obtained by integration over ω_p . Movies S1 and S2 demonstrate the spectra as a function of $\{\omega_a, \omega_b\}$, scanning ω_p as a function of time (V1) and also integrating as a function of time (V1). The desired dispersive features are expressed also by summing ω_p , justifying the 2D presentation in Fig. 5. An ultrashort pump induces large exchange asymmetry in addition to its broad frequency range coverage.

SUPPLEMENTARY MATERIALS

Supplementary material for this article is available at <https://science.org/doi/10.1126/sciadv.abj4566>

[View/request a protocol for this paper from Bio-protocol.](#)

REFERENCES AND NOTES

- M. G. Raymer, A. H. Marcus, J. R. Widom, D. L. P. Vitullo, Entangled photon-pair two-dimensional fluorescence spectroscopy (EPP-2DFS). *J. Phys. Chem. B* **117**, 15559–15575 (2013).
- J. Lavoie, T. Landes, A. Tamimi, B. J. Smith, A. H. Marcus, M. G. Raymer, Phase-modulated interferometry, spectroscopy, and refractometry using entangled photon pairs. *Adv. Quant. Technol.* **3**, 1900114 (2020).
- S. Asban, K. E. Dorfman, S. Mukamel, Interferometric spectroscopy with quantum light: Revealing out-of-time-ordering correlators. *J. Chem. Phys.* **154**, 210901 (2021).
- K. E. Dorfman, S. Asban, B. Gu, S. Mukamel, Hong-Ou-Mandel interferometry and spectroscopy using entangled photons. *Commun. Phys.* **4**, 49 (2021).

5. S. Szoke, H. Liu, B. P. Hickam, M. He, S. K. Cushing, Entangled light–matter interactions and spectroscopy. *J. Mater. Chem. C* **8**, 10732–10741 (2020).
6. S. Mukamel, M. Freyberger, W. Schleich, M. Bellini, A. Zavatta, G. Leuchs, C. Silberhorn, R. W. Boyd, L. L. Sánchez-Soto, A. Stefanov, M. Barbieri, A. Paterova, L. Krivitsky, S. Schwartz, K. Tamasaku, K. Dorfman, F. Schlawin, V. Sandoghdar, M. Raymer, A. Marcus, O. Varnavski, T. Goodson III, Z. Y. Zhou, B. S. Shi, S. Asban, M. Scully, G. Agarwal, T. Peng, A. V. Sokolov, Z. D. Zhang, M. S. Zubairy, I. A. Vartanyants, E. del Valle, F. Laussy, Roadmap on quantum light spectroscopy. *J. Phys. B Atom. Mol. Opt. Phys.* **53**, 072002 (2020).
7. C. K. Hong, L. Mandel, Theory of parametric frequency down conversion of light. *Phys. Rev. A* **31**, 2409–2418 (1985).
8. E. Bocquillon, V. Freulon, J.-M. Berroir, P. Degiovanni, B. Plaçais, A. Cavanna, Y. Jin, G. Fève, Coherence and indistinguishability of single electrons emitted by independent sources. *Science* **339**, 1054–1057 (2013).
9. de C. Chamon, D. E. Freed, S. A. Kivelson, S. L. Sondhi, X. G. Wen, Two point-contact interferometer for quantum Hall systems. *Phys. Rev. B* **55**, 2331–2343 (1997).
10. C. Déprez, L. Veyrat, H. Vignaud, G. Nayak, K. Watanabe, T. Taniguchi, F. Gay, H. Sellier, B. Sacépé, A tunable Fabry–Pérot quantum Hall interferometer in graphene. *Nat. Nanotechnol.* **16**, 555–562 (2021).
11. D. Branning, W. P. Grice, R. Erdmann, I. A. Walmsley, Engineering the indistinguishability and entanglement of two photons. *Phys. Rev. Lett.* **83**, 955–958 (1999).
12. A. S. Davydov, The theory of molecular excitons. *Soviet Physics Uspekhi* **7**, 145–178 (1964).
13. M. Khalil, A. Tokmakoff, Signatures of vibrational interactions in coherent two-dimensional infrared spectroscopy. *Chem. Phys.* **266**, 213–230 (2001).
14. S. Mukamel, *Principles of Nonlinear Optical Spectroscopy* (Oxford Univ. Press, 1995).
15. C. K. Law, I. A. Walmsley, J. H. Eberly, Continuous frequency entanglement: Effective finite hilbert space and entropy control. *Phys. Rev. Lett.* **84**, 5304–5307 (2000).
16. W. P. Grice, I. A. Walmsley, Spectral information and distinguishability in type-II down-conversion with a broadband pump. *Phys. Rev. A* **56**, 1627–1634 (1997).
17. F. Schlawin, S. Mukamel, Photon statistics of intense entangled photon pulses. *J. Phys. B Atom. Mol. Opt. Phys.* **46**, 175502 (2013).
18. A. Bahabad, M. M. Murnane, H. C. Kapteyn, Quasi-phase-matching of momentum and energy in nonlinear optical processes. *Nat. Photonics* **4**, 570–575 (2010).
19. B. Yurke, S. L. McCall, J. R. Klauder, Su(2) and Su(1,1) interferometers. *Phys. Rev. A* **33**, 4033–4054 (1986).
20. F. R. J. M. Jauch, *The Theory of Photons and Electrons* (Springer, Berlin, 1976).
21. R. D. Mota, M. A. Xicoténcatl, V. D. Granados, Jordan–Schwinger map, 3D harmonic oscillator constants of motion, and classical and quantum parameters characterizing electromagnetic wave polarization. *J. Phys. A Math. Gen.* **37**, 2835–2842 (2004).
22. R. D. Mota, M. A. Xicoténcatl, V. D. Granados, Two-dimensional isotropic harmonic oscillator approach to classical and quantum stokes parameters. *Can. J. Phys.* **82**, 767–773 (2004).
23. R. D. Mota, D. Ojeda-Guillén, M. Salazar-Ramírez, V. D. Granados, SU(1,1) approach to stokes parameters and the theory of light polarization. *J. Opt. Soc. Am. B* **33**, 1696–1701 (2016).
24. S. Mukamel, Partially-time-ordered Schwinger-Keldysh loop expansion of coherent nonlinear optical susceptibilities. *Phys. Rev. A* **77**, 023801 (2008).
25. K. E. Dorfman, S. Mukamel, Multidimensional spectroscopy with entangled light: Loop vs ladder delay scanning protocols. *New J. Phys.* **16**, 033013 (2014).
26. F. Schlawin, S. Mukamel, Two-photon spectroscopy of excitons with entangled photons. *J. Chem. Phys.* **139**, 244110 (2013).
27. K. E. Dorfman, F. Schlawin, S. Mukamel, Stimulated raman spectroscopy with entangled light: Enhanced resolution and pathway selection. *J. Phys. Chem. Lett.* **5**, 2843–2849 (2014).
28. C. K. Hong, Z. Y. Ou, L. Mandel, Measurement of subpicosecond time intervals between two photons by interference. *Phys. Rev. Lett.* **59**, 2044–2046 (1987).
29. D. Branning, W. Grice, R. Erdmann, I. A. Walmsley, Interferometric technique for engineering indistinguishability and entanglement of photon pairs. *Phys. Rev. A* **62**, 013814 (2000).
30. M. F. Limonov, M. V. Rybin, A. N. Poddubny, Y. S. Kivshar, Fano resonances in photonics. *Nat. Photonics* **11**, 543–554 (2017).
31. C. A. Marx, U. Harbola, S. Mukamel, Nonlinear optical spectroscopy of single, few, and many molecules: Nonequilibrium green’s function qed approach. *Phys. Rev. A* **77**, 022110 (2008).
32. H. C. W., *Quantum Detection and Estimation Theory* (Elsevier, Academic Press, 1976).
33. V. Giovannetti, S. Lloyd, L. Maccone, Quantum-enhanced measurements: Beating the standard quantum limit. *Science* **306**, 1330–1336 (2004).
34. V. Giovannetti, S. Lloyd, L. Maccone, Advances in quantum metrology. *Nat. Photonics* **5**, 222–229 (2011).
35. M. Napolitano, M. W. Mitchell, Nonlinear metrology with a quantum interface. *New J. Phys.* **12**, 093016 (2010).
36. M. Napolitano, M. Koschorreck, B. Dubost, N. Behbood, R. J. Sewell, M. W. Mitchell, Interaction-based quantum metrology showing scaling beyond the Heisenberg limit. *Nature* **471**, 486–489 (2011).
37. M. Howells, T. Beetz, H. Chapman, C. Cui, J. Holton, C. Jacobsen, J. Kirz, E. Lima, S. Marchesini, H. Miao, D. Sayre, D. Shapiro, J. Spence, D. Starodub, An assessment of the resolution limitation due to radiation-damage in x-ray diffraction microscopy. *J. Electron Spectros. Relat. Phenomena* **170**, 4–12 (2009).
38. O. Roslyak, C. A. Marx, S. Mukamel, Nonlinear spectroscopy with entangled photons: Manipulating quantum pathways of matter. *Phys. Rev. A* **79**, 033832 (2009).
39. K. E. Dorfman, F. Schlawin, S. Mukamel, Nonlinear optical signals and spectroscopy with quantum light. *Rev. Mod. Phys.* **88**, 045008 (2016).
40. H. J. Kimble, M. Dagenais, L. Mandel, Photon antibunching in resonance fluorescence. *Phys. Rev. Lett.* **39**, 691–695 (1977).
41. S. W. Hell, J. Wichmann, Breaking the diffraction resolution limit by stimulated emission: Stimulated-emission-depletion fluorescence microscopy. *Opt. Lett.* **19**, 780–782 (1994).
42. S. Mouradian, F. N. C. Wong, J. H. Shapiro, Achieving sub-rayleigh resolution via thresholding. *Opt. Express* **19**, 5480–5488 (2011).
43. O. Schwartz, J. M. Levitt, R. Tenne, S. Itzhakov, Z. Deutsch, D. Oron, Superresolution microscopy with quantum emitters. *Nano Lett.* **13**, 5832–5836 (2013).
44. R. Tenne, U. Rossman, B. Rephael, Y. Israel, A. Krupinski-Ptaszek, R. Lapkiewicz, Y. Silberberg, D. Oron, Super-resolution enhancement by quantum image scanning microscopy. *Nat. Photonics* **13**, 116–122 (2019).
45. J. Javanainen, P. L. Gould, Linear intensity dependence of a two-photon transition rate. *Phys. Rev. A* **41**, 5088–5091 (1990).
46. D.-I. Lee, T. Goodson, Entangled photon absorption in an organic porphyrin dendrimer. *J. Phys. Chem. B* **110**, 25582–25585 (2006).
47. A. R. Guzman, M. R. Harpham, Ö. Süzer, M. M. Haley, T. G. Goodson III, Spatial control of entangled two-photon absorption with organic chromophores. *J. Am. Chem. Soc.* **132**, 7840–7841 (2010).
48. E. Lantz, P.-A. Moreau, F. Devaux, Optimizing the signal-to-noise ratio in the measurement of photon pairs with detector arrays. *Phys. Rev. A* **90**, 063811 (2014).
49. E. Bolduc, D. Faccio, J. Leach, Acquisition of multiple photon pairs with an EMCCD camera. *J. Optics* **19**, 054006 (2017).
50. M. Reichert, H. Defienne, J. W. Fleischer, Massively parallel coincidence counting of high-dimensional entangled states. *Sci. Rep.* **8**, 7925 (2018).
51. V. Giovannetti, L. Maccone, J. H. Shapiro, F. N. C. Wong, Generating entangled two-photon states with coincident frequencies. *Phys. Rev. Lett.* **88**, 183602 (2002).
52. O. Kuzucu, F. N. C. Wong, S. Kurimura, S. Tovstolon, Joint temporal density measurements for two-photon state characterization. *Phys. Rev. Lett.* **101**, 153602 (2008).
53. S. Asban, S. Mukamel, Scattering-based geometric shaping of photon-photon interactions. *Phys. Rev. Lett.* **123**, 260502 (2019).
54. S. Asban, F. J. Garcia de Abajo, Generation, characterization, and manipulation of quantum correlations in electron beams. *npj Quantum Inf.* **7**, 42 (2021).

Acknowledgments

Funding: The support of the National Science Foundation (NSF) grant CHE-1953045 is acknowledged. **Author contributions:** S.A. and S.M. have contributed equally to this work. **Competing interests:** The authors declare that they have no competing interests. **Data and materials availability:** The main results of this manuscript are composed of analytical and numerical calculations. All data needed to evaluate the conclusions in the paper are present in the paper and/or the Supplementary Materials.

Submitted 13 May 2021

Accepted 2 August 2021

Published 22 September 2021

10.1126/sciadv.abj4566

Citation: S. Asban, S. Mukamel, Distinguishability and “which pathway” information in multidimensional interferometric spectroscopy with a single entangled photon-pair. *Sci. Adv.* **7**, eabj4566 (2021).

Distinguishability and “which pathway” information in multidimensional interferometric spectroscopy with a single entangled photon-pair

Shahaf AsbanShaul Mukamel

Sci. Adv., 7 (39), eabj4566. • DOI: 10.1126/sciadv.abj4566

View the article online

<https://www.science.org/doi/10.1126/sciadv.abj4566>

Permissions

<https://www.science.org/help/reprints-and-permissions>

Use of think article is subject to the [Terms of service](#)

Supplementary Materials for

Distinguishability and “which pathway” information in multidimensional interferometric spectroscopy with a single entangled photon-pair

Shahaf Asban* and Shaul Mukamel*

*Corresponding author. Email: sasban@uci.edu (S.A.); smukamel@uci.edu (S.M.)

Published 22 September 2021, *Sci. Adv.* 7, eabj4566 (2021)
DOI: 10.1126/sciadv.abj4566

The PDF file includes:

Supplementary Text
Figs. S1 to S3
Movies S1 and S2
Sections S1 to S6

Other Supplementary Material for this manuscript includes the following:

Movies S1 and S2

Part I

The setup and signal

S1 The Setup

We consider an entangled photon pair generated by a type-II parametric down conversion process pumped by an ultrashort pulse, such as the one reported in Ref. [14]. The pair exchange symmetry is further manipulated by a Michelson interferometer denoted U_θ in Fig. 1 (main text), which controls the degree of distinguishability [11]. The U_θ process is reviewed in detail below. After the Michelson state-preparation stage, the two photons interact with the sample, and detected via a Hong-Ou-Mandel (HOM) interferometer. The photons are first separated using a polarization beam splitter, then inserted into a HOM interferometer with variable delay T , and measured in coincidence. The corresponding signal is given by Eq. S3.

S1.1 θ -symmetrized amplitude

The Michelson interferometer operation in Fig. 1 (main text) can be described by an operator transformation (Heisenberg picture) or a by wavefunction (Schrödinger picture). We will employ the wavefunction transformation for the preparation interferometry basis and inverse field transformations from the detection basis – describing the entire process in the interaction-region. All field operators of the propagator are then given in the interaction domain. This significantly simplifies the computations by reducing the number of terms for high order processes. The reason is as follows: each field operator transformation is presented by a two-mode superposition ($SU(2)$ rotation), this implies that by rotating the frame to the interaction-mode basis, there are fewer field combinations with increasing perturbation order compared to the rotated basis. In addition, intensity detection is represented by two field operators per mode, thus, when we rotate the frame to the one in which the light-matter interaction occurs the number of contributions increases. While the result is eventually independent on the basis of choice, elimination of irrelevant processes is most convenient in the interaction frame, which is therefore adopted throughout this work.

We consider the input state (described below) generated by the modified Michelson interferometer depicted in Fig. 1b (main text), following [11]. A pump beam is reflected by a dichroic mirror (DM) then generates an entangled photon-pair denoted as *signal* and *idler* using a BBO (β - barium borate) crystal, described by the two-photon amplitude $\phi(\omega_a, \omega_b)$. The beam is superimposed using a beam splitter, and each arm is then manipulated separately. On one arm the polarizations are swapped using a $\lambda/4$ plate, while the other undergoes a controlled path delay, thus introducing θ . In the second passing through the BBO crystal, due to exchanged polarizations caused by the $\lambda/4$ plate, the two-photon amplitude is flipped from $\phi(\omega_a, \omega_b)$ to $\phi(\omega_b, \omega_a)$. The transmitted part of the beam from the DM is then given by the θ -symmetrized amplitude,

$$\Phi_{\theta}(\omega_a, \omega_b) = \frac{1}{\sqrt{2}} [\phi(\omega_a, \omega_b) + e^{i\theta} \phi(\omega_b, \omega_a)]. \quad (\text{S1})$$

Finally, the two-photon wave-function is given by

$$|\Psi_{\theta}\rangle = \int d\omega_a d\omega_b \Phi_{\theta}(\omega_a, \omega_b) a^{\dagger}(\omega_a) b^{\dagger}(\omega_b) |\text{vac}\rangle. \quad (\text{S2})$$

S1.2 The Signal & Contributing Events

The signal is defined by coincidence-counting of photons (with no further gating) at the output ports of the HOM interferometer in Fig. 1 of the main text, and formally expressed as

$$\mathcal{C}(\theta, T) = \int_{-\infty}^{\infty} \int_{-\infty}^{\infty} dt d\tau \left\langle \mathcal{T} \hat{\mathcal{O}}(t, \tau) e^{-\frac{i}{\hbar} \int_{-\infty}^{t^*} ds H_{\text{int},-}(s)} \right\rangle, \quad (\text{S3})$$

$$\hat{\mathcal{O}}(t, \tau) = E_{a',R}^{\dagger}(\mathbf{r}_a, t) E_{b',R}^{\dagger}(\mathbf{r}_b, t + \tau) E_{b',L}(\mathbf{r}_b, t + \tau) E_{a',L}(\mathbf{r}_a, t). \quad (\text{S4})$$

Here θ is the photon-pair exchange phase determined in the preparation stage, T is a relative path delay of the photons and t^* is the latest time. The superoperator notation allows us to express the observable in this compact form. Here \mathcal{T} is the time ordering superoperator which rearranges all following superoperators such that time increases from right to left. $H_{\text{int},-}$ is the interaction superoperator defined by its action on Hilbert space operator A as $H_{\text{int},-}A \equiv H_{\text{int}}A - AH_{\text{int}}$, where H_{int} is the Hilbert-space interaction Hamiltonian $H_{\text{int}} = \mathbf{E}^{\dagger} \cdot \mathbf{V} + \text{H.c.}$, and V is the dipole operator. Note that the observable is obtained by an annihilation of a photon at the detector, and thus solely defined by EM field annihilation superoperators from the right and left of the density operator, corresponding to $E_R\rho \equiv E\rho$ and $E_L\rho \equiv \rho E$. When the auxiliary system (light probe) undergoes transformations such as interferometry – $SU(2)$ rotations – the interaction and the detection are represented in different basis sets. One can compute the signal in terms of *order of arrival* of the probed photons. Alternatively, a more compact expression can be obtained by using the basis set determined by the *order of interaction*. We therefore transform the observable in Eq. S4 to the basis set in which the interaction occurs (non-primed subscripts) to obtain

$$\begin{aligned} \hat{\mathcal{O}}(t, \tau) &= E_{a,R}^{\dagger}(\mathbf{r}_a, t) E_{b,R}^{\dagger}(\mathbf{r}_b, t + \tau) E_{b,L}(\mathbf{r}_b, t + \tau) E_{a,L}(\mathbf{r}_a, t) \\ &+ E_{b,R}^{\dagger}(\mathbf{r}_a, t) E_{a,R}^{\dagger}(\mathbf{r}_b, t + \tau) E_{a,L}(\mathbf{r}_b, t + \tau) E_{b,L}(\mathbf{r}_a, t) \\ &- E_{a,R}^{\dagger}(\mathbf{r}_a, t) E_{b,R}^{\dagger}(\mathbf{r}_b, t + \tau) E_{a,L}(\mathbf{r}_b, t + T + \tau) E_{b,L}(\mathbf{r}_a, t - T) \\ &- E_{b,R}^{\dagger}(\mathbf{r}_a, t - T) E_{a,R}^{\dagger}(\mathbf{r}_b, t + T + \tau) E_{b,L}(\mathbf{r}_b, t + \tau) E_{a,L}(\mathbf{r}_a, t). \end{aligned} \quad (\text{S5})$$

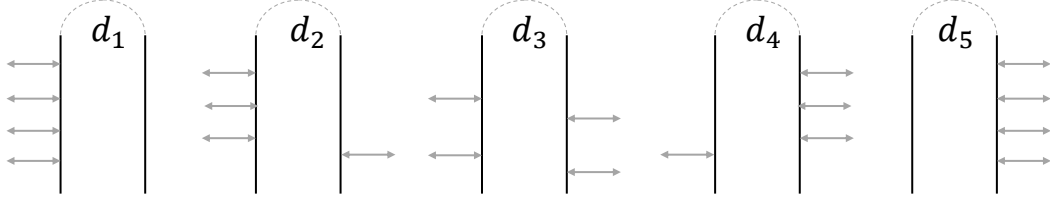


Figure S1: **Diagrammatic representation of possible processes in $\chi^{(3)}$.** The Interaction diagrams sketched terminated with dashed lines (top), represent the processes contributing to the classical $\chi^{(3)}$. Not all contribute to the coincidence-count.

This observable represents the HOM signal and can be further simplified. Since t and τ are symmetric integration variables, we can reduce the number of terms by simple time translations and conjugation to yield

$$\hat{\mathcal{O}}'(t, \tau) = 2E_{a,R}^\dagger(\mathbf{r}_a, t) E_{b,R}^\dagger(\mathbf{r}_b, t + \tau) E_{b,L}(\mathbf{r}_b, t + \tau) E_{a,L}(\mathbf{r}_a, t) - \left[E_{a,R}^\dagger(\mathbf{r}_a, t) E_{b,R}^\dagger(\mathbf{r}_b, t + \tau) E_{a,L}(\mathbf{r}_b, t + T + \tau) E_{b,L}(\mathbf{r}_a, t - T) + H.c. \right] \quad (\text{S6})$$

The observable in Eq. S6 is depicted diagrammatically in Fig. S2b, where we identify the two detection paths as non-delayed path (NDP) and delayed path (DP) respectively. Since the signal is sensitive to the participation of both modes, the lowest order nonvanishing contribution in Eq. S3 includes four light-matter interactions corresponding to the absorption and emission of both photons. The contributing processes are shown in Fig. S1, and appear in the definition of $\chi^{(3)}$ as shown in Ref. [23]. Two-photon coincidence-detection reduces the number of diagrams contributing to the signal. Only processes in which both mode E_a and E_b are detected are counted as detection events. This restricts the measurement onto a subspace of the density operator, resulting in the processes depicted in Fig. S2a.

Part II

The total coincidence-counting

S2 Contributing Processes

The signal Eq. S3 is given by $\mathcal{C}(\theta, T) = \mathcal{S}^{(I)} + \mathcal{S}^{(II)}$ where $\mathcal{S}^{(I/II)}$ corresponds to the respective set of diagrams in Fig. S2; $\mathcal{S}^{(I)}$ corresponds to the single sided diagrams $D_{1-1} - D_{1-3}$, and $\mathcal{S}^{(II)}$ to diagrams $D_{2-1} - D_{2-4}$ which contain interactions from both branches of the loop. It is possible to simplify this expression when $\Phi_{ab}^{a'b'} = \Phi_{ba}^{b'a'}$. This is the case here since

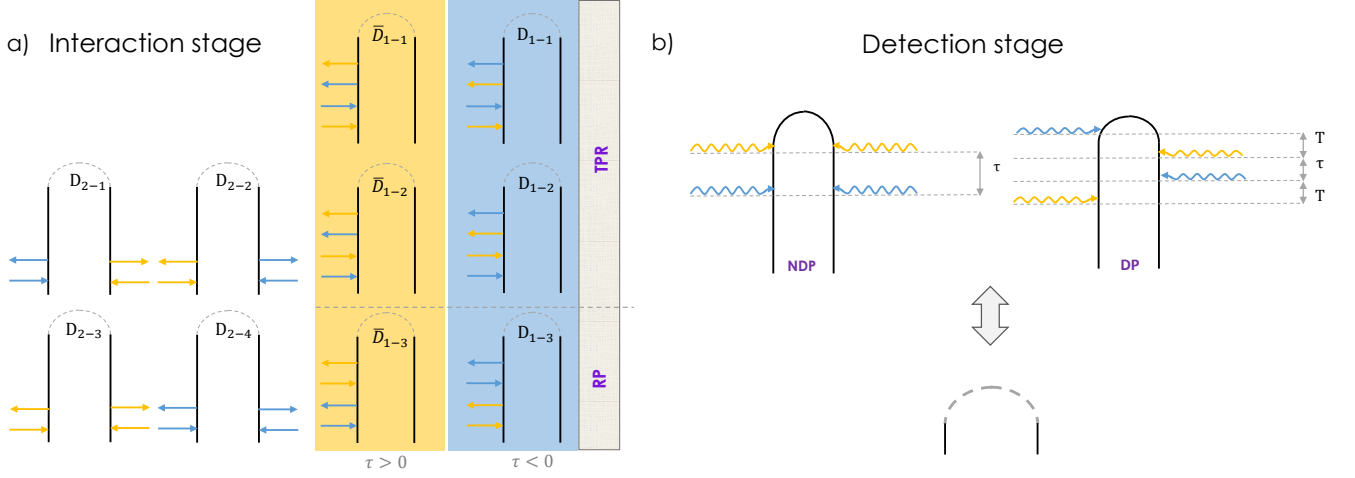


Figure S2: **Contributing processes to the HOM spectroscopic signal.** (a) The coincidence detection focuses on two-photon subspace of the density operator, thus eliminate some of the contributions to $\chi^{(3)}$. The remaining processes can be divided into three categories: two photon resonance (TPR) and Raman processes (RP). Diagrams with dashed lines on top represent the light-matter interaction part of the complete loop diagram – terminated with a detection process (NDP/DP). (b) The detection diagrams represent the possible detection loop diagram terminations. They describe coincidence detection described by annihilation of modes at the detection plane. This loop diagram representation exhibits relative shift in the detection ordering between left and right field superoperators, corresponding to the relative delays in Eq. S6

$\Phi_{\theta}^*(\omega'_a, \omega'_b) \Phi_{\theta}(\omega_a, \omega_b) = \Phi_{\theta}^*(\omega'_b, \omega'_a) \Phi_{\theta}(\omega_b, \omega_a)$ for the θ -symmetrized amplitude (it depends on $\cos(\theta)$ which is symmetric under reflection). Following the derivation in the appendices, we obtain the coincidence signal which is 4th order in the dipole operator V . This is the lowest order that includes interaction with both photons, single photon outputs do not contribute in coincidence detection, only processes terminated with two populated photons in the field contribute. These processes include two interactions per photon – absorption and emission $\propto VV^{\dagger}$ resulting in two classes of 4th order contributions $VV^{\dagger}VV^{\dagger}$ and $VVV^{\dagger}V^{\dagger}$. Expanding Eq. S3 we obtain

$$\begin{aligned}
\mathcal{S}^{(I)}(\theta, T) = 8\mathcal{J} \left\{ \int d\omega'_a d\omega'_b d\omega_a d\omega_b \delta(\omega_a + \omega_b - \omega'_a - \omega'_b) \right. \\
\times \left\{ \langle V [G(\omega'_a) + G(\omega'_b)] V G(\omega_a + \omega_b) V^{\dagger} [G(\omega_a) + G(\omega_b)] V^{\dagger} \rangle [1 - \cos(\omega_{ab}T)] \Phi_{a'b'}^{\theta*} \Phi_{ab}^{\theta} \right. \\
\left. + \langle V G(\omega'_b) V^{\dagger} [G(\omega'_b - \omega_b) - G^{\dagger}(\omega'_b - \omega_b)] V G(\omega_a) V^{\dagger} \rangle [\Phi_{ab}^{\theta} - \Phi_{ba}^{\theta} \cos(\omega_{ab}T)] \Phi_{a'b'}^{\theta*} \right\} \\
\left. \right\} \quad (S7)
\end{aligned}$$

where $\Phi_{ab}^{\theta} \equiv \Phi_{\theta}(\omega_a, \omega_b)$, and

$$\begin{aligned} \mathcal{S}^{(II)}(\theta, T) = & 8\Re \left\{ \int d\omega_a d\omega_b \langle VG^\dagger(\omega_a) V^\dagger [|\Phi_{ab}|^2 - [iG(T)] \Phi_{ba}^{\theta*} \Phi_{ab}^\theta e^{i\omega_{ab}T}] VG(\omega_a) V^\dagger \rangle \right\} \\ & - 8\Im \left\{ \int d\omega'_a d\omega'_b d\omega_a d\omega_b \delta(\omega_a + \omega_b - \omega'_a - \omega'_b) [\Phi_{ab}^\theta - \Phi_{ba}^\theta \cos(\omega_{ab}T)] \Phi_{a'b'}^{\theta*} \right. \\ & \left. \times \langle VG^\dagger(\omega'_b) V^\dagger [[G(\omega'_b - \omega_b) - G^\dagger(\omega'_b - \omega_b)] VG(\omega_a) V^\dagger] \rangle \right\}. \end{aligned}$$

See Sec. S6 for the full diagram-based derivation. We notice a sign difference between the similar expressions in both contributions. This is a result of the backward propagator in the double sided diagram. The overall coincidence signal given by $\mathcal{C}(\theta, T) = \mathcal{S}^{(I)} + \mathcal{S}^{(II)}$ then reads

$$\begin{aligned} \mathcal{C}(\theta, T) = & 8\Re \left\{ \int d\omega_a d\omega_b \underbrace{\langle VG^\dagger(\omega_a) V^\dagger [|\Phi_{ab}|^2 - \Phi_{ba}^{\theta*} \Phi_{ab}^\theta (iG(T) e^{i\omega_{ab}T})] VG(\omega_a) V^\dagger \rangle}_{D_3} \right\} \\ & + 8\Im \left\{ \int d\omega'_a d\omega'_b d\omega_a d\omega_b \delta(\omega_a + \omega_b - \omega'_a - \omega'_b) \right. \\ & \times \left\{ \underbrace{\langle V[G(\omega'_a) + G(\omega'_b)] VG(\omega_a + \omega_b) V^\dagger [G(\omega_a) + G(\omega_b)] V^\dagger \rangle}_{D_1} [1 - \cos(\omega_{a'b'}T)] \Phi_{a'b'}^{\theta*} \Phi_{ab}^\theta \right. \\ & \left. \left. + \underbrace{\langle VG(\omega'_b) V^\dagger [G(\omega'_b - \omega_b) - G^\dagger(\omega'_b - \omega_b)] VG(\omega_a) V^\dagger \rangle}_{D_2} [\cos(\omega_{ab}T) - \cos(\omega_{a'b}T)] \Phi_{a'b'}^{\theta*} \Phi_{ba}^\theta \right\} \right\}. \end{aligned} \quad (\text{S8})$$

Here, D_1 , D_2 and D_3 correspond to the diagrams in Fig. 3b of the main text.

Remark : The Green function can be computed in Hilbert space using $G(\omega) = (\omega - H + i\epsilon)^{-1}$, or in Liouville space using $\mathcal{G}(\omega) = (\omega - L + i\epsilon)^{-1}$ [23]. The reason they are the same, is that Hilbert space Green's function is defined with the ground-state energy $G_H(\omega) = (\omega + \omega_g - H + i\epsilon)^{-1}$. In this case since all interactions are written as left superoperators, the Liouvillian is always $L = H - \omega_g$ ($\hbar = 1$) – thus the expressions are identical. This is also supported by the results of Ref. [24].

S2.1 Moment generating function and relaxation dynamics

The signal includes time-domain matter Green's function that depends on of the delay $-iG(T) = \theta(T) e^{-iHT}$. It is possible to use it to study the moments of H in the small T expansion. For $T > 0$ one can write

$$e^{-i(H-\omega_{ab})T} = \sum_{n=0}^{\infty} \frac{[-i(H-\omega_{ab})T]^n}{n!},$$

expressing how the HOM signal deviates from zero with increasing T . One can measure moments of the Hamiltonian by

$$\frac{n!}{(-i)^n} \frac{\partial^n}{\partial T^n} \mathcal{C}(\theta, T) |_{T=0^+},$$

which in the degenerate case ($\omega_a = \omega_b = \omega_p/2$) results in $\propto \langle VG^\dagger(\omega) V^\dagger [H^n] VG(\omega) V^\dagger \rangle$. Such expansion can be used to study the system's coupling with the environment.

Probing dephasing dynamics

In the degenerate case ($\omega_a = \omega_b = \omega_p/2$), a single term originating from the Raman process survives in Eq. S8. It is possible to follow the dephasing dynamics of the ground state of the system as further detailed in the main text. Under these conditions we arrive at Eq. 8 in the main text

$$\mathcal{C}[\Lambda_I] \propto \Re \text{tr} \left\{ VG^\dagger \left(\frac{\omega_p}{2} \right) V^\dagger [\mathbb{1} - iG(T)] VG \left(\frac{\omega_p}{2} \right) V^\dagger \rho_\mu(-\infty) \right\}. \quad (\text{S9})$$

Expressed in terms of sum-over-states, we obtain

$$\mathcal{C}[\Lambda_I] \propto \Re \sum_{e, e' g'} \frac{1}{\frac{\omega_p}{2} - \omega_{e'g'} - i\gamma_{e'g'}} \frac{1}{\frac{\omega_p}{2} - \omega_{eg} + i\gamma_{eg}} \langle g' | [\mathbb{1} - iG(T)] | g' \rangle, \quad (\text{S10})$$

where we have used the shorthand notation $g \equiv g_1$ for the lowest energy. Eq. S10 demonstrates that the short-lived excited-states serve as a prefactor to the relaxation process of the ground state manifold, and modulate them in time domain as shown in Fig. 5c of the main text. Reminder: our definition for Green's function in Hilbert-space includes the lowest energy, assuming the form $G_H(\omega) = (\omega + \omega_g - H + i\epsilon)^{-1}$. Therefore the $\omega_{g'g}$ transitions are resolved.

S3 Pathway selectivity by exchange-phase-cycling

Taking the Fourier transform of Eq. S8 with respect to T we obtain

$$\begin{aligned}
\mathcal{D}_\theta [\Omega] &= \int dT \mathcal{C}_\theta [T] e^{i\Omega T} = 4 \int d\omega_a d\omega_b \\
&\times \left\{ 2 |\Phi_{ab}|^2 \langle VG^\dagger(\omega_a) V^\dagger VG(\omega_a) V^\dagger \rangle \delta(\Omega) \right. \\
&- \Phi_{ba}^{\theta*} \Phi_{ab}^\theta \langle VG^\dagger(\omega_a) V^\dagger [iG(\Omega + \omega_{ab}) - iG^\dagger(\Omega + \omega_{ab})] VG(\omega_a) V^\dagger \rangle \\
&+ 8\mathfrak{J} \left\{ \int d\omega'_a d\omega'_b d\omega_a d\omega_b \delta[\omega_a + \omega_b - \omega'_a - \omega'_b] \right. \\
&\times \left[\frac{1}{2} \langle VG(\omega'_b) VG(\omega_a + \omega_b) V^\dagger [G(\omega_a) + G(\omega_b)] V^\dagger \rangle [2\delta(\Omega) - \delta(\Omega - \omega_{ab}) - \delta(\Omega + \omega_{ab})] \Phi_{a'b'}^{\theta*} \Phi_{ab}^\theta \right. \\
&+ \langle VG(\omega'_b) V^\dagger [G(\omega'_b - \omega_b) - G^\dagger(\omega'_b - \omega_b)] VG(\omega_a) V^\dagger \rangle \\
&\left. \left. \times [\delta(\Omega - \omega_{ab'}) + \delta(\Omega + \omega_{ab'}) - \delta(\Omega - \omega_{ab}) - \delta(\Omega + \omega_{ab})] \Phi_{a'b'}^{\theta*} \Phi_{ba}^\theta \right\}.
\end{aligned}$$

For $\Omega = \omega_{ab} \neq 0$ we find that the RP contributions are integrated using an exchanged photon index, $\Phi_{a'b'}^{\theta*} \Phi_{ba}^\theta$ and the TPR using regular ordering $\Phi_{a'b'}^{\theta*} \Phi_{ab}^\theta$. This is useful when the exchange parity is controlled using $\theta = 0, \pi$. We break down these contributions into two functionals

$$\begin{aligned}
F_{\text{RP}} [\Omega] &= -8\pi\mathfrak{J} \int d\omega_a d\omega_b \Phi_{ba}^{\theta*} \Phi_{ab}^\theta \langle VG^\dagger(\omega_a) V^\dagger G(\Omega + \omega_{ab}) VG(\omega_a) V^\dagger \rangle \\
&+ 8\pi\mathfrak{J} \left\{ \int d\omega'_a d\omega'_b d\omega_a d\omega_b \delta[\omega_a + \omega_b - \omega'_a - \omega'_b] \Phi_{a'b'}^{\theta*} \Phi_{ba}^\theta \right. \\
&+ \langle VG(\omega'_b) V^\dagger [G(\omega'_b - \omega_b) - G^\dagger(\omega'_b - \omega_b)] VG(\omega_a) V^\dagger \rangle \\
&\left. \times [\delta(\Omega - \omega_{ab'}) + \delta(\Omega + \omega_{ab'}) - \delta(\Omega - \omega_{ab}) - \delta(\Omega + \omega_{ab})] \right\}
\end{aligned}$$

and

$$\begin{aligned}
F_{\text{TPR}} [\Omega] &= +8\pi\mathfrak{J} \left\{ \int d\omega'_a d\omega'_b d\omega_a d\omega_b \delta[\omega_a + \omega_b - \omega'_a - \omega'_b] \Phi_{a'b'}^{\theta*} \Phi_{ab}^\theta \right. \\
&\left. \times [\langle VG(\omega'_b) VG(\omega_a + \omega_b) V^\dagger [G(\omega_a) + G(\omega_b)] V^\dagger \rangle [-\delta(\Omega - \omega_{ab}) - \delta(\Omega + \omega_{ab})]] \right\}
\end{aligned}$$

such that $\mathcal{C}_\theta [\Omega] = F_{\text{TPR}} [\Omega] + F_{\text{RP}} [\Omega]$. Writing the amplitude explicitly

$$\Phi_{a'b'}^{\theta*} \Phi_{ab}^\theta = (\phi_{a'b'} + e^{-i\theta} \phi_{b'a'}) (\phi_{ab} + e^{i\theta} \phi_{ba}) = \phi_{a'b'} \phi_{ab} + \phi_{b'a'} \phi_{ba} + e^{i\theta} \phi_{a'b'} \phi_{ba} + e^{-i\theta} \phi_{b'a'} \phi_{ab}$$

$$\Phi_{a'b'}^{\theta*} \Phi_{ba}^\theta = (\phi_{a'b'} + e^{-i\theta} \phi_{b'a'}) (\phi_{ba} + e^{i\theta} \phi_{ab}) = \phi_{a'b'} \phi_{ba} + \phi_{b'a'} \phi_{ab} + e^{i\theta} \phi_{a'b'} \phi_{ab} + e^{-i\theta} \phi_{b'a'} \phi_{ba}$$

The relative sign between the two contributions depends on θ , we thus obtain

$$\begin{pmatrix} \mathcal{D}_0[\Omega] \\ \mathcal{D}_\pi[\Omega] \end{pmatrix} = \begin{pmatrix} 1 & 1 \\ 1 & -1 \end{pmatrix} \begin{pmatrix} F_{\text{TPR}}[\Omega] \\ F_{\text{RP}}[\Omega] \end{pmatrix}, \quad (\text{S11})$$

or inverted

$$\begin{pmatrix} F_{\text{TPR}}[\Omega] \\ F_{\text{RP}}[\Omega] \end{pmatrix} = \frac{1}{2} \begin{pmatrix} 1 & 1 \\ 1 & -1 \end{pmatrix} \begin{pmatrix} \mathcal{D}_0[\Omega] \\ \mathcal{D}_\pi[\Omega] \end{pmatrix}, \quad (\text{S12})$$

where $\mathcal{D}_{0,\pi}[\Omega]$ correspond to $\theta = 0, \pi$ respectively. In the main text, we follow a similar procedure for the more elaborate detection scheme that includes frequency information and detailed below.

Part III

Frequency-resolved coincidence-counting

S4 setup and observable

We now consider a more elaborate detection scheme, denoted as U_D^{II} in the main text. The two photons are frequency dispersed, then measured in coincidence at known frequency. The signal is defined by

$$\mathcal{C}(\omega_a, \omega_b, \theta, T) = \left\langle \mathcal{T} \hat{\mathcal{O}}(\omega_a, \omega_b) e^{-\frac{i}{\hbar} \int_{-\infty}^{t^*} ds H_{\text{int},-}(s)} \right\rangle, \quad (\text{S13})$$

$$\hat{\mathcal{O}}(\omega_a, \omega_b) = E_{a',R}^\dagger(\mathbf{r}_a, \omega_a) E_{b',R}^\dagger(\mathbf{r}_b, \omega_b) E_{b',L}(\mathbf{r}_b, \omega_b) E_{a',L}(\mathbf{r}_a, \omega_a). \quad (\text{S14})$$

We define the diagrammatic expansion using the temporal expressions, by introducing the Fourier transforms $\mathbf{E}(\mathbf{r}_i, \omega_i) = \int dt \mathbf{E}(\mathbf{r}_i, t) e^{i\omega_i t}$, then consider all possible time ordering of photon arrivals,

$$\begin{aligned} \mathcal{C}(\omega_a, \omega_b, \theta, T) &= \int dt_1 dt_2 dt_3 dt_4 e^{i\omega_a(t_4-t_1)} e^{i\omega_b(t_3-t_2)} \\ &\times \left\langle \mathcal{T} \mathbf{E}_{a'}^\dagger(\mathbf{r}_a, t_1) \mathbf{E}_{b'}^\dagger(\mathbf{r}_b, t_2) \mathbf{E}_{b'}(\mathbf{r}_b, t_3) \mathbf{E}_{a'}(\mathbf{r}_a, t_4) e^{-\frac{i}{\hbar} \int_{-\infty}^{t^*} ds H_{\text{int},-}(s)} \right\rangle. \quad (\text{S15}) \end{aligned}$$

Transforming the fields in the frequency to the interaction-plane in frequency domain is obtained by the inverse HOM transformation with the respective exchange phase factor, the observable then takes the form

$$\hat{\mathcal{O}}(\omega_a, \omega_b) = E_a^\dagger(\omega_a) E_b^\dagger(\omega_b) E_b(\omega_b) E_a(\omega_a) - e^{-i\omega_{ab}T} E_a^\dagger(\omega_b) E_b^\dagger(\omega_a) E_b(\omega_b) E_a(\omega_a) + H.c. \quad (\text{S16})$$

where we have expressed it using Hilbert-space operators and omitted the spatial coordinates for brevity. The path related phase is already adopted using the temporal coordinate and we can assume equal propagation lengths in what follows. We can write this expression explicitly,

$$\begin{aligned} \mathcal{C}(\omega_a, \omega_b, \theta, T) &= 2\Re \int dt_1 dt_2 dt_3 dt_4 e^{i\omega_a(t_4-t_1)} e^{i\omega_b(t_3-t_2)} \\ &\times \left\langle \mathcal{T} \mathbf{E}_a^\dagger(\mathbf{r}_a, t_1) \mathbf{E}_b^\dagger(\mathbf{r}_b, t_2) \mathbf{E}_b(\mathbf{r}_b, t_3) \mathbf{E}_a(\mathbf{r}_a, t_4) e^{-\frac{i}{\hbar} \int_{-\infty}^{t^*} ds H_{\text{int},-}(s)} \right\rangle_{(\text{NDP})} \\ &- 2\Re e^{-i\omega_{ab}T} \int dt_1 dt_2 dt_3 dt_4 e^{i\omega_a(t_4-t_2)} e^{i\omega_b(t_3-t_1)} \\ &\times \left\langle \mathcal{T} \mathbf{E}_a^\dagger(\mathbf{r}_a, t_1) \mathbf{E}_b^\dagger(\mathbf{r}_b, t_2) \mathbf{E}_b(\mathbf{r}_b, t_3) \mathbf{E}_a(\mathbf{r}_a, t_4) e^{-\frac{i}{\hbar} \int_{-\infty}^{t^*} ds H_{\text{int},-}(s)} \right\rangle_{(\text{DP})}, \quad (\text{S17}) \end{aligned}$$

where the division between the DP's and NDPs is reflected by the exchanged time coordinates in the Fourier transform. Two-photon contributions to this detection scheme are given by

$$\begin{aligned} \mathcal{S}^{(1)}(\omega_a, \omega_b, \theta, T) &= 4\Im \left\{ \int d\omega_1 d\omega_2 \delta(\omega_a + \omega_b - \omega_1 - \omega_2) \right. \\ &\times [\Phi_{a,b}^{\theta*} [1 - \cos(\omega_{ab}T)] \Phi_{1,2}^\theta \langle V [G(\omega_a) + G(\omega_b)] V G(\omega_a + \omega_b) V^\dagger [G(\omega_1) + G(\omega_2)] V^\dagger \rangle \\ &+ [\Phi_{a,b}^{\theta*} - \Phi_{b,a}^{\theta*} \cos(\omega_{ab}T) \Phi_{1,2}^\theta] \\ &\times [\langle V G(\omega_b) V^\dagger G(\omega_b - \omega_2) V G(\omega_1) V^\dagger \rangle + \langle V G(\omega_a) V^\dagger G(\omega_a - \omega_1) V G(\omega_2) V^\dagger \rangle] \left. \right\} \quad (\text{S18}) \end{aligned}$$

and

$$\begin{aligned}
\mathcal{S}^{(\text{II})}(\omega_a, \omega_b, \theta, T) = & -2\Im \left\{ \right. \\
& \left[\int d\omega \Phi_{\omega,b}^\theta [\Phi_{\omega,b}^{\theta*} - \Phi_{b,\omega}^{\theta*} e^{-i\omega_{ab}T}] \langle VG^\dagger(\omega) V^\dagger [G(\omega - \omega_a) - G^\dagger(\omega - \omega_a)] VG(\omega) V^\dagger \rangle \right. \\
& \left. + \int d\omega \Phi_{a,\omega}^\theta [\Phi_{a,\omega}^{\theta*} - \Phi_{\omega,a}^{\theta*} e^{-i\omega_{ab}T}] \langle VG^\dagger(\omega) V^\dagger [G(\omega - \omega_b) - G^\dagger(\omega - \omega_b)] VG(\omega) V^\dagger \rangle \right] \\
& - 4\Im \left\{ \int d\omega \Phi_{\omega+\omega_{ab},b}^\theta [\Phi_{a,\omega}^{\theta*} - \Phi_{\omega,a}^{\theta*} e^{-i\omega_{ab}T}] \right. \\
& \left. \times \langle VG^\dagger(\omega) V^\dagger [G(\omega - \omega_b) - G^\dagger(\omega - \omega_b)] VG(\omega + \omega_{ab}) V^\dagger \rangle \right\}. \tag{S19}
\end{aligned}$$

The total signal is given by $\mathcal{C}_\theta(\omega_a, \omega_b, T) = \mathcal{S}^{(\text{I})}(\omega_a, \omega_b, \theta, T) + \mathcal{S}^{(\text{II})}(\omega_a, \omega_b, \theta, T)$, used in the exchange-phase-cycling protocols illustrated in Fig. 5 of the main text and elaborated Below in Sec. S5.

S4.1 Sum-over-states expressions

2D spectroscopic signals for our model system are given by the sum-over-states expressions. Introducing the dipole operator,

$$V = \sum_{b>a} \mu_{ab} |b\rangle \langle a|, \tag{S20}$$

in the matter energy eigenbasis, we can express both contributions of the coincidence signal in Eqs. S18 and S19

$$\begin{aligned}
\mathcal{S}^{(\text{I})}(\omega_a, \omega_b, \theta, T) = & 4\Im \left\{ \int d\omega_1 d\omega_2 \delta(\omega_a + \omega_b - \omega_1 - \omega_2) \right. \\
& \times [\Phi_{a,b}^{\theta*} [1 - \cos(\omega_{ab}T)] \Phi_{1,2}^\theta \{ F_{\text{DQC}}[\omega_a, \omega_a + \omega_b, \omega_1] + F_{\text{DQC}}[\omega_b, \omega_a + \omega_b, \omega_1] \\
& \quad F_{\text{DQC}}[\omega_a, \omega_a + \omega_b, \omega_2] + F_{\text{DQC}}[\omega_b, \omega_a + \omega_b, \omega_2] \} \\
& \left. + [\Phi_{a,b}^{\theta*} - \Phi_{b,a}^{\theta*} \cos(\omega_{ab}T)] \Phi_{1,2}^\theta F_{\text{RP}}^{(I)}[\omega_b, \omega_b - \omega_2, \omega_1] + F_{\text{RP}}^{(I)}[\omega_a, \omega_a - \omega_1, \omega_2] \right\}, \tag{S21}
\end{aligned}$$

and

$$\begin{aligned}
\mathcal{S}^{(II)}(\omega_a, \omega_b, \theta, T) = & -2\Im \left\{ \right. \\
& \left[\int d\omega \Phi_{\omega,b}^\theta [\Phi_{\omega,b}^{\theta*} - \Phi_{b,\omega}^{\theta*} e^{-i\omega_{ab}T}] \left\{ F_{\text{RP}}^{(II.1)}[\omega, \omega - \omega_a, \omega] - F_{\text{RP}}^{(II.2)}[\omega, \omega - \omega_a, \omega] \right\} \right. \\
& + \int d\omega \Phi_{a,\omega}^\theta [\Phi_{a,\omega}^{\theta*} - \Phi_{\omega,a}^{\theta*} e^{-i\omega_{ab}T}] \left\{ F_{\text{RP}}^{(II.1)}[\omega, \omega - \omega_b, \omega] - F_{\text{RP}}^{(II.2)}[\omega, \omega - \omega_b, \omega] \right\} \\
& - 4\Im \left\{ \int d\omega \Phi_{\omega+\omega_{ab},b}^\theta [\Phi_{a,\omega}^{\theta*} - \Phi_{\omega,a}^{\theta*} e^{-i\omega_{ab}T}] \right. \\
& \left. \left. \times \left\{ F_{\text{RP}}^{(II.1)}[\omega, \omega - \omega_b, \omega + \omega_{ab}] - F_{\text{RP}}^{(II.2)}[\omega, \omega - \omega_b, \omega + \omega_{ab}] \right\} \right\} \right. \\
& \left. \right\}. \tag{S22}
\end{aligned}$$

where the total signal is given by

$$\mathcal{C}[\Lambda_{II}] = \mathcal{S}^{(I)}(\omega_a, \omega_b, \theta, T) + \mathcal{S}^{(II)}(\omega_a, \omega_b, \theta, T), \tag{S23}$$

in terms of the following auxiliary functions

$$\begin{aligned}
F_{\text{TPR}}[\omega_1, \omega_2, \omega_3] &= \sum_{e,e',f} \frac{\mu_{ge}\mu_{ef}\mu_{f'e'}\mu_{e'g}}{(\omega_1 - \omega_{eg} + i\gamma_{eg})(\omega_2 - \omega_{fg} + i\gamma_{fg})(\omega_3 - \omega_{e'g} + i\gamma_{e'g})} \\
F_{\text{RP}}^{(I)}[\omega_1, \omega_2, \omega_3] &= \sum_{e,e',g'} \frac{\mu_{ge}\mu_{eg'}\mu_{g'e'}\mu_{e'g}}{(\omega_1 - \omega_{eg} + i\gamma_{eg})(\omega_2 - \omega_{g'g} + i\gamma_{g'g})(\omega_3 - \omega_{e'g} + i\gamma_{e'g})} \\
F_{\text{RP}}^{(II.1)}[\omega_1, \omega_2, \omega_3] &= \sum_{e,e',g'} \frac{\mu_{ge}\mu_{eg'}\mu_{g'e'}\mu_{e'g}}{(\omega_1 - \omega_{eg} + i\gamma_{eg})(\omega_2 - \omega_{g'g} + i\gamma_{g'g})(\omega_3 - \omega_{e'g} - i\gamma_{e'g})} \\
F_{\text{RP}}^{(II.2)}[\omega_1, \omega_2, \omega_3] &= \sum_{e,e',g'} \frac{\mu_{ge}\mu_{eg'}\mu_{g'e'}\mu_{e'g}}{(\omega_1 - \omega_{eg} + i\gamma_{eg})(\omega_2 - \omega_{g'g} - i\gamma_{g'g})(\omega_3 - \omega_{e'g} - i\gamma_{e'g})}. \tag{S24}
\end{aligned}$$

In the main text we have defined the following auxiliary functionals to express the cycling protocol in a convenient manner

$$\begin{aligned}
\Xi_{\text{TPR}} = & 4 \left\{ \int d\omega_1 d\omega_2 \delta(\omega_a + \omega_b - \omega_1 - \omega_2) \right. \\
& \times [\Phi_{a,b}^{\theta*} [1 - \cos(\omega_{ab}T)] \Phi_{1,2}^\theta \{ F_{\text{DQC}}[\omega_a, \omega_a + \omega_b, \omega_1] + F_{\text{DQC}}[\omega_b, \omega_a + \omega_b, \omega_1] \\
& \left. F_{\text{DQC}}[\omega_a, \omega_a + \omega_b, \omega_2] + F_{\text{DQC}}[\omega_b, \omega_a + \omega_b, \omega_2] \} \right. \\
& \left. \right\} \tag{S25}
\end{aligned}$$

$$\left. \right\} \tag{S26}$$

and

$$\begin{aligned}
\Xi_{\text{RP}} = & -4 \left\{ \int d\omega \Phi_{\omega+\omega_{ab},b}^\theta [\Phi_{a,\omega}^{\theta*} - \Phi_{\omega,a}^{\theta*} e^{-i\omega_{ab}T}] \right. \\
& \times \left\{ F_{\text{RP}}^{(II.1)} [\omega, \omega - \omega_b, \omega + \omega_{ab}] - F_{\text{RP}}^{(II.2)} [\omega, \omega - \omega_b, \omega + \omega_{ab}] \right\} \\
& - 2 \left\{ \left[\int d\omega \Phi_{\omega,b}^\theta [\Phi_{\omega,b}^{\theta*} - \Phi_{b,\omega}^{\theta*} e^{-i\omega_{ab}T}] \left\{ F_{\text{RP}}^{(II.1)} [\omega, \omega - \omega_a, \omega] - F_{\text{RP}}^{(II.2)} [\omega, \omega - \omega_a, \omega] \right\} \right. \right. \\
& + \left. \int d\omega \Phi_{a,\omega}^\theta [\Phi_{a,\omega}^{\theta*} - \Phi_{\omega,a}^{\theta*} e^{-i\omega_{ab}T}] \left\{ F_{\text{RP}}^{(II.1)} [\omega, \omega - \omega_b, \omega] - F_{\text{RP}}^{(II.2)} [\omega, \omega - \omega_b, \omega] \right\} \right. \\
& + 4 \left\{ \int d\omega_1 d\omega_2 \delta(\omega_a + \omega_b - \omega_1 - \omega_2) \right. \\
& \times \left. \left[\Phi_{a,b}^{\theta*} - \Phi_{b,a}^{\theta*} \cos(\omega_{ab}T) \right] \Phi_{1,2}^\theta F_{\text{RP}}^{(I)} [\omega_b, \omega_b - \omega_2, \omega_1] + F_{\text{RP}}^{(I)} [\omega_a, \omega_a - \omega_1, \omega_2] \right\} \left. \right\}, \tag{S27}
\end{aligned}$$

These functionals encapsulate a process-specific information, without specifying whether the real or imaginary parts are taken, leaving θ, ω_{ab} and T to be determined in the definitions of $\mathcal{C}_\theta(\eta)$ and \mathcal{D}_θ , where $\eta = (\omega_a - \omega_b)T$. The exchange-phase-cycling protocols interfere between Ξ_i to obtain path-selective contributions as shown in Eqs. 10a-d in the main text.

S5 Cycling protocols

It is possible to extract the real and imaginary parts of the response, and further separate the various contributions by using cycling protocols. These are not unique, there are multiple choices of linearly-dependent cycling protocols to achieve path selectivity. Here, we provide one example resulting in the 2D spectra presented in Fig. S3a-e. It is convenient to denote pathway specific auxiliary functions Ξ_{TPR} and Ξ_{RP} as done in the main text, encapsulating all the diagrams that contribute to each of the respective pathways and explicitly defined

$$\mathcal{I}_{\text{TPR}}(\omega_a, \omega_b) = \mathcal{C}_\pi(\pi) \tag{S28a}$$

$$\mathcal{R}_{\text{TPR}}(\omega_a, \omega_b) = \mathcal{D}_{\frac{\pi}{2}} - \mathcal{D}_{-\frac{\pi}{2}} - \mathcal{C}_{\frac{\pi}{2}}(0) + \mathcal{C}_{-\frac{\pi}{2}}(0) + \mathcal{C}_{\frac{\pi}{2}}\left(\frac{\pi}{2}\right) - \mathcal{C}_{-\frac{\pi}{2}}\left(\frac{\pi}{2}\right) \tag{S28b}$$

$$\mathcal{I}_{\text{RP}}(\omega_a, \omega_b) = \mathcal{C}_{\frac{\pi}{2}}(0) + \mathcal{C}_{+\frac{\pi}{2}}(0) \tag{S28c}$$

$$\mathcal{R}_{\text{RP}}(\omega_a, \omega_b) = \mathcal{C}_{\frac{\pi}{2}}(0) - \mathcal{C}_{\frac{\pi}{2}}(0), \tag{S28d}$$

where $\mathcal{D}_\theta = \int dT e^{-i\Omega T} \mathcal{C}_\theta(\eta)$. These expressions depend heavily on the asymmetry of the entangled beam, which is compatible with ultrashort pump pulse. The selectivity of the response of both contributions seem to depend on the asymmetric part of the amplitude consistently. This can be explained in the following way – for vanishing lifetime broadening, all Green functions

result in delta functions multiplied by a factor of i . This means that the imaginary part of the integrated response is actually the real-part of matter correlation function. Similarly, the real part corresponds to the imaginary part of the correlation function – introducing phase shift between optical modes that are associated with losses. When the entangled pair is symmetric to exchange, it is not possible to distinguish between loss and gain events which erodes the ability to reconstruct the matter temporal dynamics. Complementarily, when the entangled pair is highly asymmetric to exchange, the information which photon emitted first is imprinted in the signal, and improves the ability to reconstruct the temporal information. This implies that entangled photons generated by an ultrafast pump, are imprinted with information that permits temporal resolution despite their extended temporal profile as individual photons. On the other hand, entangled pair generated by CW pump does not contain such information. This means that the temporal properties are inherited from the generating beam and allows to reconstruct when measure simultaneously.

The constructed antisymmetric JSA Φ_π is 'blind' to two consecutive transitions of equal frequency (degenerate). While this eliminates the resolution of such transitions, they are visible in the joint signal framework (non-selective), as demonstrated in Fig. S3. This is obtained by the cycling protocol $\mathcal{C}_0(\pi)$ corresponding to equal RP and TPR contributions. The symmetric construction Φ_0 ensures the resolution of degenerate processes (lacking the real part of the response).

The propagator $G(\omega_1 - \omega_a)$ in $\mathcal{S}^{(1)}$ takes both positive and negative frequencies – hinting that out-of-time-ordering contributions in the time domain may be involved. These type of fascinating correlation functions occur in interferometric quantum spectroscopic setups, introducing new type of wave-mixing signals [1]. Furthermore, the Raman pathways can be employed to scan for states which are forbidden for dipole transition directly from the initial (ground) state. By fixing $\omega = \omega_p - \omega_b$ in the narrowband regime resonant with $|1\rangle \rightarrow |3\rangle$ transition, and $\omega_a = \omega_{32}$ resonant with the transition $|2\rangle_{\text{forbidden}} \leftrightarrow |3\rangle$.

Part IV

Diagram-specific contributions

S6 Contributing processes to Eq. S8

First, we define the integral operators for the trace over the field degrees of freedom, which operate to the right on $f(\omega_{a/b})$ according to rules

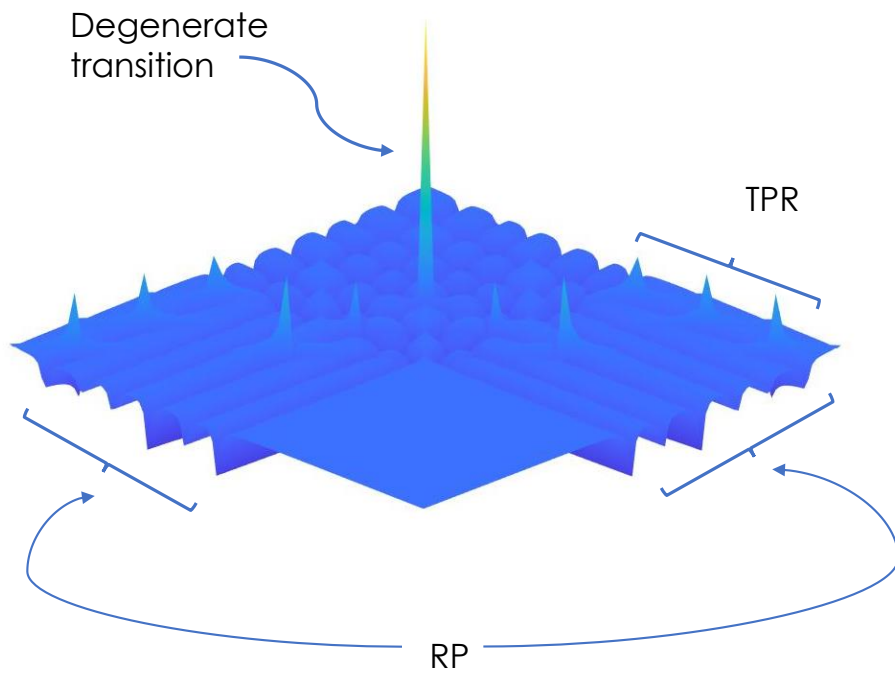


Figure S3: Degenerate transition resolution.

$$\Phi \xrightarrow{a'b'} f(\omega_{a/b}) \equiv \int d\omega'_a d\omega'_b d\omega_a d\omega_b \Phi_\theta^*(\omega'_a, \omega'_b) \Phi_\theta(\omega_a, \omega_b) f(\omega_{a/b}), \quad (\text{S29a})$$

$$\Phi \xrightarrow{a'b'} f(\omega_{a/b}) \equiv \int d\omega'_a d\omega'_b d\omega_a d\omega_b \Phi_\theta^*(\omega'_a, \omega'_b) \Phi_\theta(\omega_a, \omega_b) \delta[(\omega_a + \omega_b) - (\omega'_a + \omega'_b)] f(\omega_{a/b}), \quad (\text{S29b})$$

$$\Phi \xrightarrow{ab} f(\omega_{a/b}) \equiv \int d\omega_a d\omega_b |\Phi_\theta(\omega_a, \omega_b)|^2 f(\omega_{a/b}), \quad (\text{S29c})$$

$$\Phi \xrightarrow{ba} f(\omega_{a/b}) \equiv \int d\omega_a d\omega_b \Phi_\theta^*(\omega_b, \omega_a) \Phi_\theta(\omega_a, \omega_b) f(\omega_{a/b}). \quad (\text{S29d})$$

With this simplified notation we obtain the solutions to the diagrams in Fig. S2. Double sided NDP contributions

$$D_{2-1}^{NDP} : \Phi \xrightarrow{a'b'} \langle VG^\dagger(\omega'_b) V^\dagger [iG(\omega'_b - \omega_b) - iG^\dagger(\omega'_b - \omega_b)] VG(\omega_a) V^\dagger \rangle \quad (\text{S30})$$

$$D_{2-2}^{NDP} : \Phi \xrightarrow{a'b'} \langle VG^\dagger(\omega'_a) V^\dagger [iG(\omega_b - \omega'_b) - iG^\dagger(\omega_b - \omega'_b)] VG(\omega_b) V^\dagger \rangle \quad (\text{S31})$$

$$D_{2-3}^{NDP} : \Phi \xrightarrow{ab} \langle VG^\dagger(\omega_a) V^\dagger VG(\omega_a) V^\dagger \rangle, \quad (\text{S32})$$

$$D_{2-4}^{NDP} : D_{2-3}^{NDP}(\omega_a \leftrightarrow \omega_b), \quad (\text{S33})$$

where the matter Green's function is defined by $G(t) = -i\theta(t) e^{-i\hat{H}t}$ and in frequency domain $G(\omega) = (\omega + \omega_g - \hat{H} + i\epsilon)^{-1}$. Double sided DP contributions for $T > 0$

$$D_{2-1}^{DP} : \Phi \xrightarrow{ba} e^{i\omega_{ab}T} \langle VG^\dagger(\omega_a) V^\dagger [iG(T)] VG(\omega_a) V^\dagger \rangle \quad (\text{S34})$$

$$D_{2-2}^{DP} : \Phi \xrightarrow{ba} e^{i\omega_{ab}T} \langle VG^\dagger(\omega_b) V^\dagger [-iG^\dagger(T)] VG(\omega_b) V^\dagger \rangle \quad (\text{S35})$$

$$D_{2-3}^{DP} : \Phi \xrightarrow{a'b'} e^{i\omega_{b'b}T} \langle VG^\dagger(\omega'_a) V^\dagger [iG(\omega_a - \omega'_b) - iG^\dagger(\omega_a - \omega'_b)] VG(\omega_a) V^\dagger \rangle \quad (\text{S36})$$

$$D_{2-4}^{DP} : \Phi \xrightarrow{a'b'} e^{i\omega_{b'b}T} \langle VG^\dagger(\omega'_b) V^\dagger [iG(\omega'_b - \omega_a) - iG^\dagger(\omega'_b - \omega_a)] VG(\omega_b) V^\dagger \rangle, \quad (\text{S37})$$

and $\omega_{ab} \equiv \omega_a - \omega_b$. Similarly, the NDPs of the one sided diagrams are given by

$$D_{1-2}^{NDP} : \Phi \xrightarrow{a'b'} \langle VG(\omega'_a) VG(\omega_a + \omega_b) V^\dagger G(\omega_a) V^\dagger \rangle, \quad (\text{S38})$$

$$\bar{D}_{1-2}^{NDP} : \Phi \xrightarrow{a'b'} \langle VG(\omega'_b) VG(\omega_a + \omega_b) V^\dagger G(\omega_b) V^\dagger \rangle, \quad (\text{S39})$$

$$D_{1-1}^{NDP} : \Phi \xrightarrow{a'b'} \langle VG(\omega'_b) VG(\omega_a + \omega_b) V^\dagger G(\omega_a) V^\dagger \rangle, \quad (\text{S40})$$

$$\bar{D}_{1-1}^{NDP} : \Phi \xrightarrow{a'b'} \langle VG(\omega'_a) VG(\omega_a + \omega_b) V^\dagger G(\omega_b) V^\dagger \rangle, \quad (\text{S41})$$

$$\bar{D}_{1-3}^{NDP} : \Phi \xrightarrow{a'b'} \langle VG(\omega'_b) V^\dagger G(\omega'_b - \omega_b) VG(\omega_a) V^\dagger \rangle, \quad (\text{S42})$$

$$D_{1-3}^{NDP} : \Phi \xrightarrow{a'b'} \langle VG(\omega'_a) V^\dagger G(\omega'_a - \omega_a) VG(\omega_b) V^\dagger \rangle, \quad (\text{S43})$$

and for the DPs, we do not specify the diagram since for $\tau < 0$ there are two contributions for each section – in which $|\tau| \geq 2T$. We therefore specify just the final expressions

$$\Phi \frac{a'b'}{ab} e^{-i\omega_{a'b'}T} \langle VG(\omega'_a) VG(\omega_a + \omega_b) V^\dagger G(\omega_b) V^\dagger \rangle, \text{(TPR)} \quad (\text{S44})$$

$$\Phi \frac{a'b'}{ab} e^{-i\omega_{a'b'}T} \langle VG(\omega'_a) VG(\omega_a + \omega_b) V^\dagger G(\omega_a) V^\dagger \rangle, \text{(TPR)} \quad (\text{S45})$$

$$\Phi \frac{a'b'}{ab} e^{-i\omega_{a'b'}T} \langle VG(\omega'_a) V^\dagger G(\omega'_a - \omega_b) VG(\omega_a) V^\dagger \rangle, \text{(RP)} \quad (\text{S46})$$

$$\Phi \frac{a'b'}{ab} e^{-i\omega_{a'b'}T} \langle VG(\omega'_b) VG(\omega_a + \omega_b) V^\dagger G(\omega_a) V^\dagger \rangle, \text{(TPR)} \quad (\text{S47})$$

$$\Phi \frac{a'b'}{ab} e^{-i\omega_{a'b'}T} \langle VG(\omega'_b) VG(\omega_a + \omega_b) V^\dagger G(\omega_b) V^\dagger \rangle, \text{(TPR)} \quad (\text{S48})$$

$$\Phi \frac{a'b'}{ab} e^{-i\omega_{a'b'}T} \langle VG(\omega'_b) V^\dagger G(\omega'_b - \omega_a) VG(\omega_b) V^\dagger \rangle. \text{(RP)} \quad (\text{S49})$$

S6.1 The coincidence counting signal

Using the double exchange invariance of the θ symmetrized amplitude – $\Phi_{ab}^{a'b'} = \Phi_{ba}^{b'a'}$ – we can obtain compact expressions for the double sided contributions using the labeling of Fig. S2

$$D_{2-1}^{NDP} + D_{2-2}^{NDP} : 2\Phi \frac{a'b'}{ab} \langle VG^\dagger(\omega'_b) V^\dagger [iG(\omega'_b - \omega_b) - iG^\dagger(\omega'_b - \omega_b)] VG(\omega_a) V^\dagger \rangle \quad (\text{S50a})$$

$$D_{2-3}^{NDP} + D_{2-4}^{NDP} : 2\Phi \frac{ab}{ab} \langle VG^\dagger(\omega_a) V^\dagger VG(\omega_a) V^\dagger \rangle, \quad (\text{S50b})$$

and

$$D_{2-1}^{DP} + D_{2-2}^{DP} : \Phi \frac{ba}{ab} e^{i\omega_{ab}T} \langle VG^\dagger(\omega_a) V^\dagger [iG(T)] VG(\omega_a) V^\dagger \rangle + c.c. \quad (\text{S50c})$$

$$D_{2-3}^{DP} + D_{2-4}^{DP} : 2\Phi \frac{a'b'}{ab} \cos(\omega_{b'b}T) \langle VG^\dagger(\omega'_b) V^\dagger [iG(\omega'_b - \omega_a) - iG^\dagger(\omega'_b - \omega_a)] VG(\omega_b) V^\dagger \rangle. \quad (\text{S50d})$$

Similarly for the single sided contributions (including their complex conjugates)

$$\bar{D}_{1-2}^{NDP} : -2i\Phi \frac{a'b'}{ab} \langle VG(\omega'_b) VG(\omega_a + \omega_b) V^\dagger G(\omega_b) V^\dagger \rangle + c.c., \quad (\text{S51a})$$

$$D_{1-1}^{NDP} : -2i\Phi \frac{a'b'}{ab} \langle VG(\omega'_b) VG(\omega_a + \omega_b) V^\dagger G(\omega_a) V^\dagger \rangle + c.c., \quad (\text{S51b})$$

$$\bar{D}_{1-3}^{NDP} : -2i\Phi \frac{a'b'}{ab} \langle VG(\omega'_b) V^\dagger G(\omega'_b - \omega_b) VG(\omega_a) V^\dagger \rangle + c.c., \quad (\text{S51c})$$

and for the DPs, we do not specify the diagram since for $\tau < 0$ there are two contributions for each section – in which $|\tau| \geq 2T$. We therefore specify just the final expressions

$$-2i\Phi \xrightarrow{a'b'}_{ab} \cos(\omega_{a'b'}T) \langle VG(\omega'_b) VG(\omega_a + \omega_b) V^\dagger G(\omega_a) V^\dagger \rangle + \text{c.c.}, \quad (\text{S51d})$$

$$-2i\Phi \xrightarrow{a'b'}_{ab} \cos(\omega_{a'b'}T) \langle VG(\omega'_b) VG(\omega_a + \omega_b) V^\dagger G(\omega_b) V^\dagger \rangle + \text{c.c.}, \quad (\text{S51e})$$

$$-2i\Phi \xrightarrow{a'b'}_{ab} \cos(\omega_{a'b'}T) \langle VG(\omega'_b) V^\dagger G(\omega'_b - \omega_a) VG(\omega_b) V^\dagger \rangle + \text{c.c.} \quad (\text{S51f})$$

Remark: there is a nontrivial background in the second order which takes the form

$$S^{(2)}(\theta, T) = 2\Re \int d\omega_a d\omega_b \left[|\Phi_{ab}^\theta|^2 - \Phi_{ba}^{\theta*} \Phi_{ab}^\theta e^{i\omega_{ab}T} \right] \times [G(\omega_a) + G(\omega_b) - G^\dagger(\omega_a) - G^\dagger(\omega_b)]. \quad (\text{S52})$$

Clearly, $S_2(0, 0) = 0$.

Similarly, diagrams D_{1-i}^* are simply derived from complex conjugation of all 12 D_{1-i} contributions. Finally, the signal is obtained by subtracting twice the DPs from twice the real part of the NDPs, $\mathcal{C}(\theta, T) = 2(\mathcal{S}_{NDP} - \Re \mathcal{S}_{DP}) = \mathcal{S}^{(I)} + \mathcal{S}^{(II)}$, where $\mathcal{S}^{(I/II)}$ corresponds to the single sided and double sided diagrams respectively. It is possible to simplify this expression when $\Phi_{ab}^{a'b'} = \Phi_{ba}^{b'a'}$. In our case it is possible since $\Phi_\theta^*(\omega'_a, \omega'_b) \Phi_\theta(\omega_a, \omega_b) = \Phi_\theta^*(\omega'_b, \omega'_a) \Phi_\theta(\omega_b, \omega_a)$ for the θ -symmetrized amplitude (it depends on $\cos(\theta)$ which is symmetric for reflection).

From the single sided diagrams we obtain

$$\begin{aligned} \mathcal{S}^{(I)}(\theta, T) = & 8\Im \left\{ \int d\omega'_a d\omega'_b d\omega_a d\omega_b \delta(\omega_a + \omega_b - \omega'_a - \omega'_b) \right. \\ & \times \left\{ \langle VG(\omega'_b) VG(\omega_a + \omega_b) V^\dagger [G(\omega_a) + G(\omega_b)] V^\dagger \rangle [1 - \cos(\omega_{a'b'}T)] \Phi_{a'b'}^{\theta*} \Phi_{ab}^\theta \right. \\ & \left. \left. + \langle VG(\omega'_b) V^\dagger [G(\omega'_b - \omega_b) - G^\dagger(\omega'_b - \omega_b)] VG(\omega_a) V^\dagger \rangle [\Phi_{ab}^\theta - \Phi_{ba}^\theta \cos(\omega_{a'b'}T)] \Phi_{a'b'}^{\theta*} \right\} \right\} \quad (\text{S53}) \end{aligned}$$

where $\Phi_{ab}^\theta \equiv \Phi_\theta(\omega_a, \omega_b)$, and from the double-sided contributions

$$\begin{aligned} \mathcal{S}^{(II)}(\theta, T) = & 8\Re \left\{ \int d\omega_a d\omega_b \langle VG^\dagger(\omega_a) V^\dagger [|\Phi_{ab}^\theta|^2 - [iG(T)] \Phi_{ba}^{\theta*} \Phi_{ab}^\theta e^{i\omega_{ab}T}] VG(\omega_a) V^\dagger \rangle \right\} \\ & - 8\Im \left\{ \int d\omega'_a d\omega'_b d\omega_a d\omega_b \delta(\omega_a + \omega_b - \omega'_a - \omega'_b) [\Phi_{ab}^\theta - \Phi_{ba}^\theta \cos(\omega_{ab}T)] \Phi_{a'b'}^{\theta*} \right. \\ & \left. \times \langle VG^\dagger(\omega'_b) V^\dagger [G(\omega'_b - \omega_b) - G^\dagger(\omega'_b - \omega_b)] VG(\omega_a) V^\dagger \rangle \right\}. \end{aligned}$$

We notice that there is a sign difference between the similar expressions in both contributions. This is a result of the backward propagator in the double sided diagram. The over all coincidence signal is given by $\mathcal{C}(\theta, T) = \mathcal{S}^{(I)} + \mathcal{S}^{(II)}$ (remember prefactors and complex conjugation as well as relative signs)

$$\begin{aligned} \mathcal{C}(\theta, T) = & 8\Re \left\{ \int d\omega_a d\omega_b \langle VG^\dagger(\omega_a) V^\dagger [|\Phi_{ab}|^2 - \Phi_{ba}^{\theta*} \Phi_{ab}^\theta (iG(T) e^{i\omega_{ab}T})] VG(\omega_a) V^\dagger \rangle \right\} \\ & + 8\Im \left\{ \int d\omega'_a d\omega'_b d\omega_a d\omega_b \delta(\omega_a + \omega_b - \omega'_a - \omega'_b) \right. \\ & \times \left\{ \langle VG(\omega'_b) VG(\omega_a + \omega_b) V^\dagger [G(\omega_a) + G(\omega_b)] V^\dagger \rangle [1 - \cos(\omega_{a'b'}T)] \Phi_{a'b'}^{\theta*} \Phi_{ab}^\theta \right. \\ & \left. \left. + \langle VG(\omega'_b) V^\dagger [G(\omega'_b - \omega_b) - G^\dagger(\omega'_b - \omega_b)] VG(\omega_a) V^\dagger \rangle [\cos(\omega_{ab'}T) - \cos(\omega_{a'b'}T)] \Phi_{a'b'}^{\theta*} \Phi_{ba}^\theta \right\} \right\}. \end{aligned} \quad (\text{S54})$$

Part V

Supplementary movies captions

Movie S1: We sweep ω_p as a function of time in the ω_a, ω_b plane. We observe the signal $\mathcal{S}_1 = -\log_{10} \{1 + \mathcal{C}_0[\pi]\}$ corresponding to Eq. 10 of the main text. Here we see the RP and parallel to the axes while the TPR processes as sharp resonances when $\omega_a + \omega_b = \omega_{fg}$.

Movie S2: We sweep and integrate along the ω_p dimension as a function of time and show the ω_a, ω_b plane. We observe the logarithmic scale coincidence signal obtained from Eq. 10 of the main text $\mathcal{S}_1 = -\log_{10} \{1 + \mathcal{C}_0[\pi]\}$. Spectral information corresponding to the RP and TPR resonances is obtained. This provides a convenient lower dimensional expression of the signal. Similar approach was used in Fig. 5 of the main text.